

ARTICLE OPEN



Record low sea ice extent in the Weddell Sea, Antarctica in April/May 2019 driven by intense and explosive polar cyclones

B. Jena¹ , C. C. Bajish¹ , J. Turner², M. Ravichandran^{1,3} , N. Anilkumar¹ and S. Kshitija¹

Sea ice extent (SIE) in the Weddell Sea attained exceptionally low levels in April (1.97 million km²) and May (3.06 million km²) 2019, with the values being ~22% below the long-term mean. Using in-situ, satellite and atmospheric reanalysis data, we show the large negative SIE anomalies were driven by the passage of a series of intense and explosive polar cyclones (with record low pressure), also known as atmospheric 'bombs', which had atmospheric rivers on their eastern flanks. These storms led to the poleward propagation of record-high swell and wind waves (~9.6 m), resulting in southward ice advection (~50 km). Thermodynamic processes also played a part, including record anomalous atmospheric heat (>138 W m⁻²) and moisture (>300 kg m⁻¹s⁻¹) fluxes from midlatitudes, along with ocean mixed-layer warming (>2 °C). The atmospheric circulation anomalies were associated with an amplified wave number three pattern leading to enhanced meridional flow between midlatitudes and the Antarctic.

npj Climate and Atmospheric Science (2022)5:19; <https://doi.org/10.1038/s41612-022-00243-9>

INTRODUCTION

The Weddell Sea sea ice cover is an important component of the Earth's climate system and influences planetary albedo, ocean-atmosphere interaction and circulation, weather patterns¹⁻³, global ocean water mass characteristics^{4,5}, ice shelf and ice sheet stability⁶, the marine-cryosphere ecosystem⁷⁻¹⁰, primary production, biogeochemical processes¹¹, and shipping/logistic operations¹². At the sea ice maximum in September, the sea ice extent (SIE) in the Weddell Sea represents ~36.7% of the total Antarctica sea ice cover, and the area contains the largest percentage of Antarctic multiyear sea ice of any sector of the Southern Ocean¹³ (Supplementary Fig. 1). Nearly four decades (1979–2020) of sea ice observations from passive microwave satellite instruments indicate a moderate increase of $0.43 \pm 0.4\%$ per decade in the Antarctic SIE with spatially variable patterns of increasing and decreasing trends in different sectors. The observed variability has been attributed to a number of complex physical processes that include atmospheric circulation associated with zonal wave number three (ZW3)¹⁴⁻¹⁹, upper ocean temperature and salinity feedback^{20,21}, regional wind driven sea ice drift²², ozone depletion, stratospheric cooling²³⁻²⁶ and large-scale surface climate oscillators such as the Southern Annular Mode (SAM) and El Niño Southern Oscillation (ENSO)²⁷⁻³³. In the recent decades, the SAM is modulated by stratospheric ozone depletion resulting surface climate change in the Antarctic and Southern Ocean²⁵. This climate change driven trend has led to intensification and poleward movement of westerly winds, upper ocean freshening and cooling of the Southern Ocean, resulting sea ice growth^{20,21,28}. Several studies using coupled climate models showed the Antarctic sea ice decline in response to increase in the SAM^{34,35}. From the research to date, it is difficult to draw definite conclusions regarding the causative physical mechanisms behind the observed sea ice changes. Therefore, the physical processes driving the sea ice changes may not be represented correctly in climate models due to complex ocean-ice-atmosphere interactions, limiting our confidence in the projections of sea ice changes over the coming decades.

Following the moderate increase in SIE from 1979 to 2015, a sudden decrease occurred in spring 2016 with the largest ice loss being in the Weddell Sea³⁶⁻³⁹. It is essential to understand the ocean-atmospheric processes that trigger such rapid declines in order to ensure their simulation in models. The Weddell Sea summer SIE and sea ice concentration (SIC) reached their minimum in 2016–2017, which was attributed to polar cyclones with record low central mean sea level pressure (MSLP), reappearance of a polynya, upper ocean warming, and westerly wind strengthening that advected multi-year ice out of the northern Weddell Sea³⁶. Several deep cyclones and ocean eddies led to divergence in the sea ice cover and to anomalously record low sea ice conditions over the Weddell Sea and Lazarev Sea. There was also the reoccurrence of a polynya in 2016 and 2017^{18,40,41}. This took place in association with an amplification of the atmospheric ZW3 pattern around Antarctica. A significant amount of heat and moisture was transported from midlatitudes through ZW3-linked atmospheric rivers that resulted in melting of Weddell Sea sea ice during 2017¹⁹.

In the Southern Hemisphere the maximum amplitude of the zonal waves is located approximately between 45°S and 50°S and the waves have an impact on the sea ice^{14,15,18,42}. An enhancement of the ZW3 feature with meridional transports of heat and moisture fluxes had significant impacts on the Antarctic sea ice through changes in surface temperature⁴³. The ZW3 pattern drives the poleward (ascending branch of troughs) and equatorward (descending branch of ridges) transport of warm and cold air¹⁵. This alignment of the planetary waves causes large temperature gradients in different sectors which aids the formation of polar cyclones near the sea ice cover^{18,44}. Therefore, on a daily time scale, the ZW3 pattern is often closely linked to the synoptic-scale extreme weather systems that influence the ice extent. The majority of earlier studies have dealt with sea ice changes driven by atmosphere and ocean circulation on interannual and decadal timescales through monthly mean observations that may suppress information on synoptic-scale changes. Therefore, it is important to

¹National Centre for Polar and Ocean Research, Ministry of Earth Sciences, Government of India, Vasco da Gama, Goa, India. ²British Antarctic Survey, Natural Environment Research Council, Cambridge, UK. ³Present address: Ministry of Earth Sciences, Government of India, New Delhi, India. ✉email: bjena@ncpor.res.in

study the synoptic-scale weather events in order to explain the interannual and decadal variability of sea ice^{33,37}.

Cyclones influence sea ice cover by advecting the ice through dynamical forcing via their warm, strong winds that can lead to both compaction and melt of sea ice. Synoptic systems are responsible for enhanced transport of heat and moisture into the Weddell Sea^{45,46} and affect the ice cover through atmospheric energy forcing from cyclones^{47,48}. In parallel, strong winds associated with the cyclones generate large ocean waves and swell which propagate poleward into the sea ice zone, breaking up the ice cover and leading to ice melt^{45,49,50}. The extensive fetch over the Weddell Sea is conducive for generation of large ocean waves that modulates interaction between ocean, atmosphere and ice cover⁵¹. Also, the Weddell Sea water column is characterized by weak static stability^{40,52} and the strong winds can induce upwelling of sub-surface warm water from circumpolar deep water masses toward the surface, preventing the formation of sea ice or melting existing sea ice⁵³. Even though the sea ice changes have been linked to polar cyclones³⁶, understanding the wave-sea ice interaction needs further investigation^{45,54}. An improved knowledge of the mechanism of polar cyclone-induced wave-sea ice interaction and ocean-atmospheric influences are important for reexamining the recent changes in Antarctic sea ice and simulating future conditions in a warming climate.

There was persistence of a large negative SIE and sea ice area (SIA) anomaly in the Weddell Sea in each summer (December, January) from 2016 to 2020 (Fig. 1a). It is not surprising that a large negative anomaly occurred in summer as there was less sea ice cover remaining for melting. However, there was also a large negative SIE and SIA anomaly during the ice growth period from April to May 2019 (Fig. 1a). The pattern of SIE variability was similar to SIA. The SIE attained its fourth lowest extent in April 2019 and the lowest extent in the satellite era in May 2019 (Fig. 1b). Here we employ in-situ, satellite and atmospheric reanalysis data to quantify the role of several intense and explosive polar cyclones (defined as the relative central pressure normalized deepening rate 'NDR,' over 24 h exceeding unity, see the method)^{45,55,56} in driving record low SIE in the Weddell Sea during April–May 2019 within the context of the whole time series of passive microwave satellite observations from 1979 to 2020. We advance from recent findings^{45,47} by quantifying the SIE variability in the Weddell Sea from February to May 2019, focusing on how the cyclone-induced dynamic and thermodynamic processes coupled with the change in ocean mixed layer played a role.

RESULTS AND DISCUSSION

Exceptional record low sea ice extent

Daily and monthly sea ice observations were analyzed for 1979–2020 to study the anomalous ice condition over the Weddell Sea during April–May 2019. The months from February to September are the period of sea ice growth in Antarctica (Supplementary Fig. 1). For example, the spatially averaged daily SIE in the Weddell Sea indicates a climatological lowest ice extent of 1.17 million km² on 21 February, followed by a gradual increase up to 6.72 million km² until 22 September (Fig. 2c, Supplementary Fig. 1). The time series of daily satellite observations (1979–2020) show the Weddell Sea SIE declined suddenly in November 2016 and negative ice anomalies predominated until June, 2020 and reappeared in December, 2020 (Fig. 1a). During 2016–2020, the large negative SIE anomaly (0.96–1.31 million km²) reoccurred early each summer from 16 to 23 December then returned to the near-climatological mean value in the early months of subsequent years when the SIE was at its lowest. Amongst these events, a large negative anomaly of SIE (1.01 × 10⁶ km²) in summer 2018–2019 returned to its climatological mean in the following autumn for a period of 7 days (4–10 March 2019) with a maximum positive

anomaly of 0.01 million km² (Fig. 1a). A further negative SIE anomaly occurred from 11 March 2019 that reached an exceptional low ice extent in April (0.63 × 10⁶ km²) and lowest ever extent (0.92 × 10⁶ km²) from 1 May to 3 June 2019. While an unprecedented low ice extent occurred in May 2019, the largest rate of change of SIE anomaly started on 31 March 2019 with the most rapid rate of decline during 16–19 April (0.032–0.038 × 10⁶ km² day⁻¹), followed by 0.026–0.034 × 10⁶ km² day⁻¹ during 31 March–4 April, 11–15 May and 22–31 May 2019 (Fig. 2c).

The monthly mean SIE in the Weddell Sea reached the fourth lowest extent on record (1.97 × 10⁶ km²) during April 2019 which was 23.3% lower than the long-term (1979–2008) mean value of 2.57 × 10⁶ km² (Fig. 1b). The lowest extent of sea ice for this period was prominently over the longitude range 14.5°W–43°W (Supplementary Fig. 2a). Further, the SIE reached the lowest ever monthly mean extent on record in May 2019 (3.06 × 10⁶ km²) which was 21.2% lower than the long-term (1979–2008) mean value of 3.89 × 10⁶ km² (Fig. 1b). The lowest extent was mainly over the longitudes 6.5°W–32°W (Supplementary Fig. 2b). Analysis of monthly composite maps indicated a dipole pattern of sea ice variability with negative anomalies established in the marginal ice zone of the Weddell Sea and positive anomalies along the coastal Lazarev Sea during February–March 2019 (Supplementary Fig. 3a). The region of negative anomalies in the Weddell Sea extended eastward across the Lazarev Sea in April and May 2019 (Supplementary Fig. 3b, c).

Polar cyclones that led to the exceptional low sea ice cover

There was a large negative SIE anomaly from 31 March 2019 that reached the lowest ever extent on record from 1 May to 3 June 2019 corresponding to the passage of a series of eleven polar cyclones including three explosive events (indicated as C3, C8, and C11 on the figures) that crossed south of 60°S over the Weddell Sea (Figs. 1a, 2a, b, Table 1). Among the eleven polar cyclones, four cyclones (C1–C4) were observed in April 2019 and seven cyclones (C5–C11) in May 2019, which together had an impact on the SIE decline (Fig. 2a–c). However, the most rapid rate of SIE decline (0.026–0.038 × 10⁶ km² day⁻¹) occurred during the passage of two cyclones (C1, C3) in April 2019 and two cyclones (C8, C11) in May 2019 that we have examined in detail.

Initiation of rapid ice decline in response to polar cyclones C1 and C2

The cyclone C1 was observed over the Weddell Sea at 18 UTC 29 March and followed a south-eastward trajectory until 4 April 2019 (Fig. 2a). This was an intense synoptic system (see the method, Atmospheric reanalysis) which deepened by >27 hPa in 24 h at 00 UTC 31 March at ~65°S ~32.5°W with a minimum central MSLP of 931 hPa (Figs. 2b, 3a, Table 1). The MSLP (wind speed) over a large area along the cyclone track on 31 March 2019 was the lowest (highest) ever recorded in the 42-year data from 1979 to 2020, indicating the very rare nature of the event (Fig. 3a). On 31 March, the cyclone C1 with a region of extremely negative central MSLP anomaly of up to ~-47.2 hPa extended over the Weddell Sea sea ice cover, accompanied by a positive pressure anomaly (~10 hPa) to its northeast (Figs. 3a, 4a, Supplementary Fig. 4a). The pressure gradient directed north to north-westerly winds with enhanced intrusion of anomalous heat and moisture flux from midlatitudes into the Weddell Sea leading to a negative SIE anomaly (Fig. 3a–c). A peak in integrated water vapor flux (IWVF) exceeding 240 kg m⁻¹s⁻¹ was observed along the track of C1 (Figs. 3c, 4c, Supplementary Fig. 4c). The feature had the characteristics of an atmospheric river¹⁹ with the cloud band extending from the south Atlantic Ocean to the Weddell Sea on 31 March 2019 (Fig. 3d). Advection of anomalous heat and moisture flux from the south Atlantic Ocean to the Weddell Sea through atmospheric river promotes

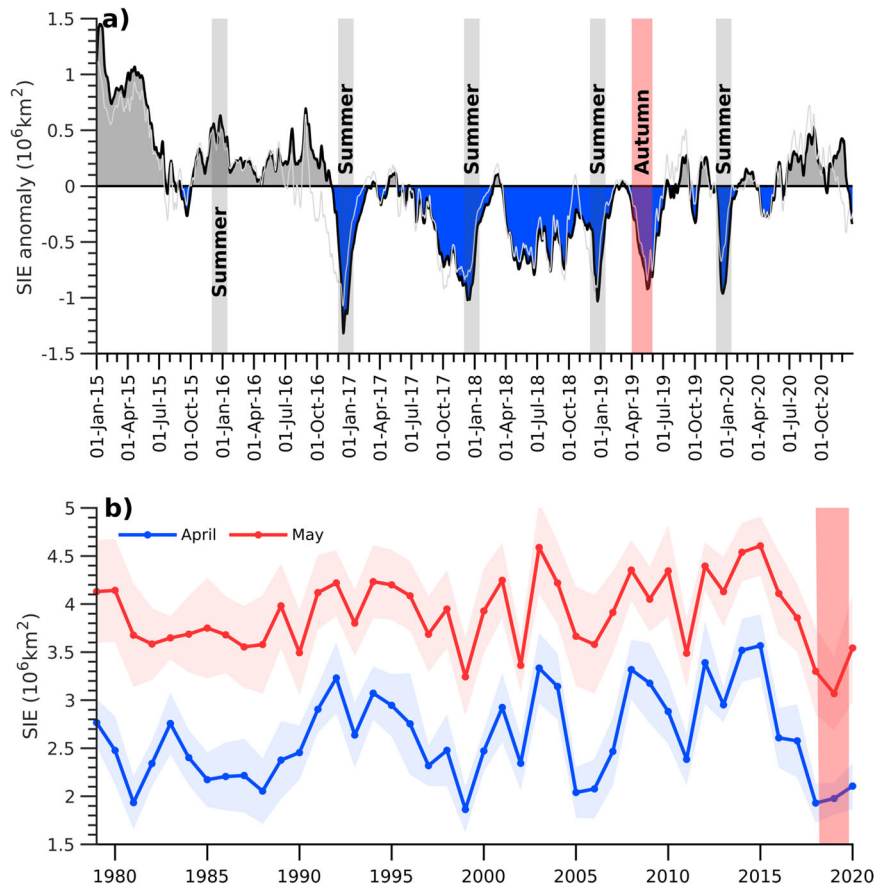


Fig. 1 Sudden declines in sea ice extent (SIE) in the Weddell Sea. **a** Daily SIE anomalies from 2015 to 2020 relative to the climatology of 1979–2008, spatially averaged from 60°W to 20°E and 55°S to the Antarctic coast (Methods section ‘Sea ice observations’). The light gray line denotes the changes in sea ice area (SIA). The negative (positive) anomalies of SIE are filled in blue (dark gray). Vertical gray-shaded bars represent the SIE anomaly in each early summer (1 December–15 January) with the largest negative values being observed from 16 to 23 December during 2016–2020. Vertical red-shaded bar represents the exceptional event of largest negative anomaly in autumn (April–May) 2019. **b** Interannual variability of mean SIE for April (blue line) and May (red line) with ± 1 standard deviation (shade) marked for each year. Vertical red-shade represents the exceptionally low SIE in April and May 2019, considering the entire time series of satellite observations starting from 1979 to 2020.

anomalous increase in downward long-wave radiation ($\sim 52 \text{ W m}^{-2}$) to the surface⁵⁷ that facilitated atmospheric warming ($r = 0.95$, Fig. 3e, Table 1, Supplementary Table 1). During this period, the magnitude of the positive anomalous surface air temperature (SAT) of up to $\sim 10^\circ\text{C}$ was observed along the eastern flank of the cyclone with a net gain of heat flux (NHf) of up to $\sim 113 \text{ W m}^{-2}$ at the ocean surface (Figs. 3b, e, 4b, c). In contrast, the western flank was associated with advection of cold air from Antarctica into the Weddell Sea (Fig. 3b, e). The strong winds on the western flank of the cyclone over the Weddell Sea led to an anomalous loss of heat flux up to $\sim 153 \text{ W m}^{-2}$ as the atmospheric temperature was relatively colder than usual. The upward oceanic heat flux into the atmosphere facilitated the anomalous growth of sea ice just to the east of Antarctic Peninsula (AP). Correspondingly, a dipole pattern of variability with anomalously negative (positive) SIC was observed from 47°W to 3°W (west of 47°W) (Fig. 3a). Also, the strong northerly (southerly) winds advected sea ice⁵⁸ poleward (equatorward), resulting in a decrease (increase) of ice extent in the eastern (western) flank of the cyclone (Fig. 3a, d). In parallel, the penetration of ocean waves from the open ocean into the sea ice zone played an important part in breaking up the ice cover^{45,49,59–61}. The cyclone C1 with strong winds of up to $\sim 22 \text{ m s}^{-1}$ triggered the generation of record high ocean waves over a large area in the Weddell Sea, which propagated southeastward into the marginal ice zone (Fig. 3f). As a result, there was a sudden growth in significant

wave height (SWH) of up to $\sim 9.64 \text{ m}$ with an anomaly of $\sim 6.57 \text{ m}$ during 31 March–4 April 2019 (Supplementary Fig. 4d). The SWH values observed near the ice edge on 31 March 2019 were the highest ever ocean waves for this day in the 42-year record from 1979 to 2020 (Fig. 3f). In such anomalous sea state conditions under the influence of cyclone C1, the ocean waves propagated into the ice-covered region likely provided adequate energy for mechanical breaking up the ice cover in the Weddell Sea. Further, the broken ice could be deformed easily by the intense cyclonic winds that induces a divergence in the sea ice cover¹⁸. Indeed, the rapid sea ice decline has strong correspondence ($r = -0.50$ to -0.64) with the intense winds and a sudden growth in SWH during the intense and explosive cyclones (Figs. 2c, 3f, 4d, Table 1, Supplementary Table 1).

Besides the aforementioned processes, the upper ocean was forced by strong negative wind stress curl with values greater than $-0.45 \times 10^{-5} \text{ N m}^{-3}$ during the passage of cyclone C1 (Figs. 3g, 4a). The water column in the Weddell Sea is normally characterized by low surface salinity and a cold-water mass separated from an underlying high-salinity warm water mass with weak static stability^{40,62}. The negative wind stress curl along the cyclone track was favorable for upwelling and mixing of sub-surface warm water into the surface layer. There was a strong negative correlation between the wind stress curl and mixed layer temperature (MLT) during the passage of the intense and explosive cyclones ($r = -0.61$, Supplementary Table 1). A record high sea surface temperature

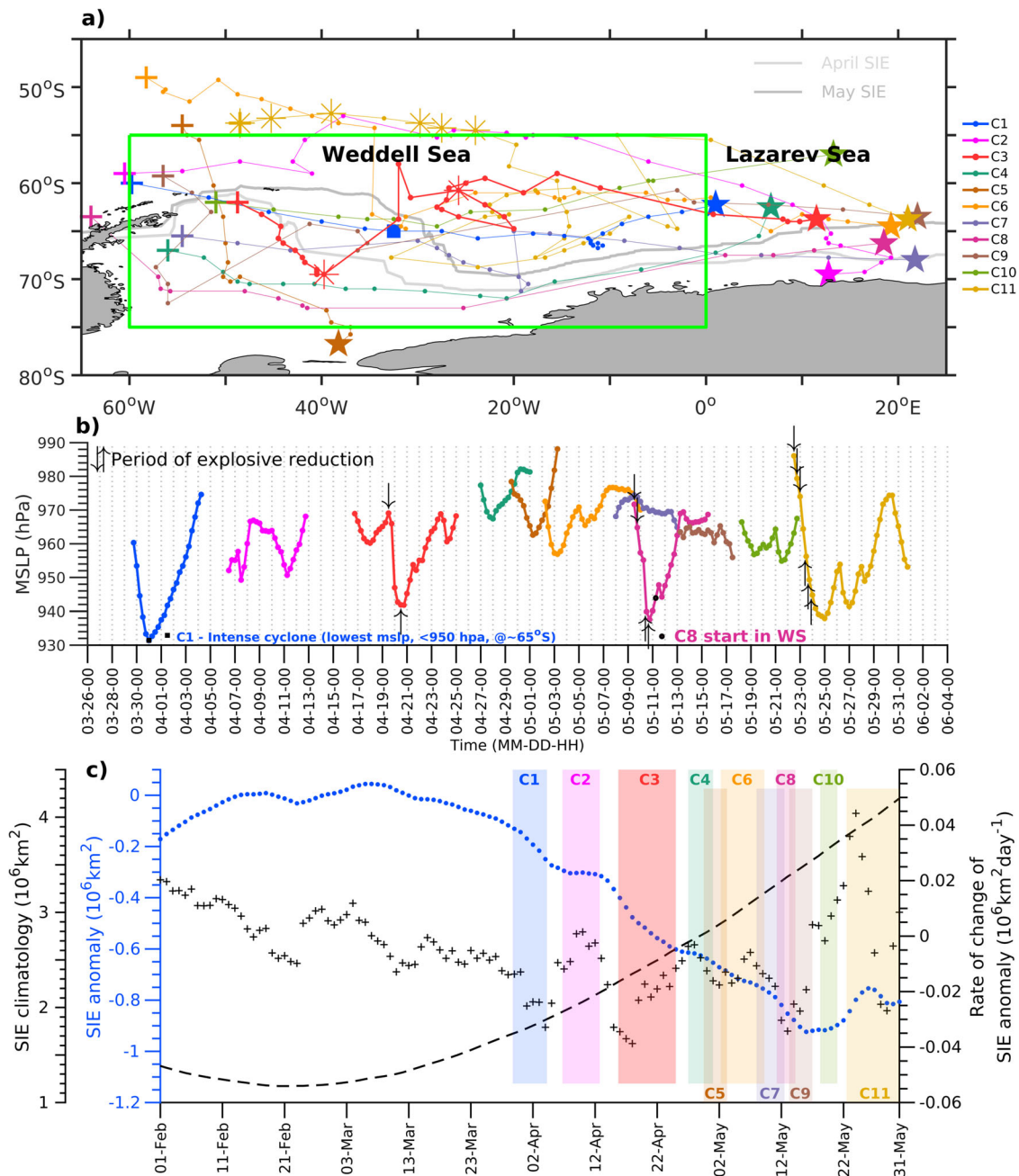


Fig. 2 Polar cyclones and sea ice extent (SIE) changes in the Weddell Sea. **a** Polar cyclone tracks during April–May 2019 are marked by lines with the dots indicating positions at 6 hourly intervals. Of the eleven cyclones (C1–C11), three systems were explosive in nature (C3, C8, C11) that formed south of 60°S in the Weddell Sea during 16–25 April 2019 (C3), 11–15 May (C8), and 22–31 May 2019 (C11). Blue square represents the location of an unusual intense cyclonic system (C1) with a record low pressure. Occurrences of explosive events are marked in asterisks. For most of the systems, the cyclolysis (stars) occurred in the Lazarev Sea. The monthly sea ice edge relative to the cyclone tracks are shown for April (light gray) and May (dark gray) 2019. **b** Life cycle of polar cyclones including intense (square) and explosive (arrows) developments (Methods section ‘Atmospheric reanalysis’). **c** Daily SIE anomalies (blue dots) from 01 February to 31 May 2019 relative to the climatology of 1979–2008 (black dashed line), spatially-averaged over the Weddell Sea from 60°W to 20°E and 55°S to Antarctic coast (Methods section ‘Sea ice observations’). Vertical shaded bars represent the occurrence period of polar cyclones corresponding to SIE anomalies. The plus marks indicate the rate of change of SIE anomaly per day and has the largest negative changes during an explosive cyclones-C3, followed by two explosive cyclone-C1, C8 and C11.

(SST) anomaly of up to $\sim +2^{\circ}\text{C}$ and mixed layer warming is evident between the low-pressure centre and bands of high wind stress associated with cyclone C1, that prevented thermodynamic growth of sea ice (Figs. 3g–h, 4b). The regions of record low MSLP were correspondingly collocated with record high wind speed, IWVF, NHF, SAT, SHW, SST and MLT, indicating the major impact of cyclone C1 on the rapid sea ice decline (Fig. 3). Even though

cyclone C1 had an immediate impact on sea ice through extreme changes in ocean–atmospheric conditions, an anomalous warming of ocean mixed layer with record high values ($>3^{\circ}\text{C}$) persisting from the previous summer (January–February 2019) continued well into the subsequent autumn (March–May 2019) and played a role in preconditioning for the negative sea ice anomalies (Fig. 4b, Supplementary Fig. 5). The ocean preconditioning followed by

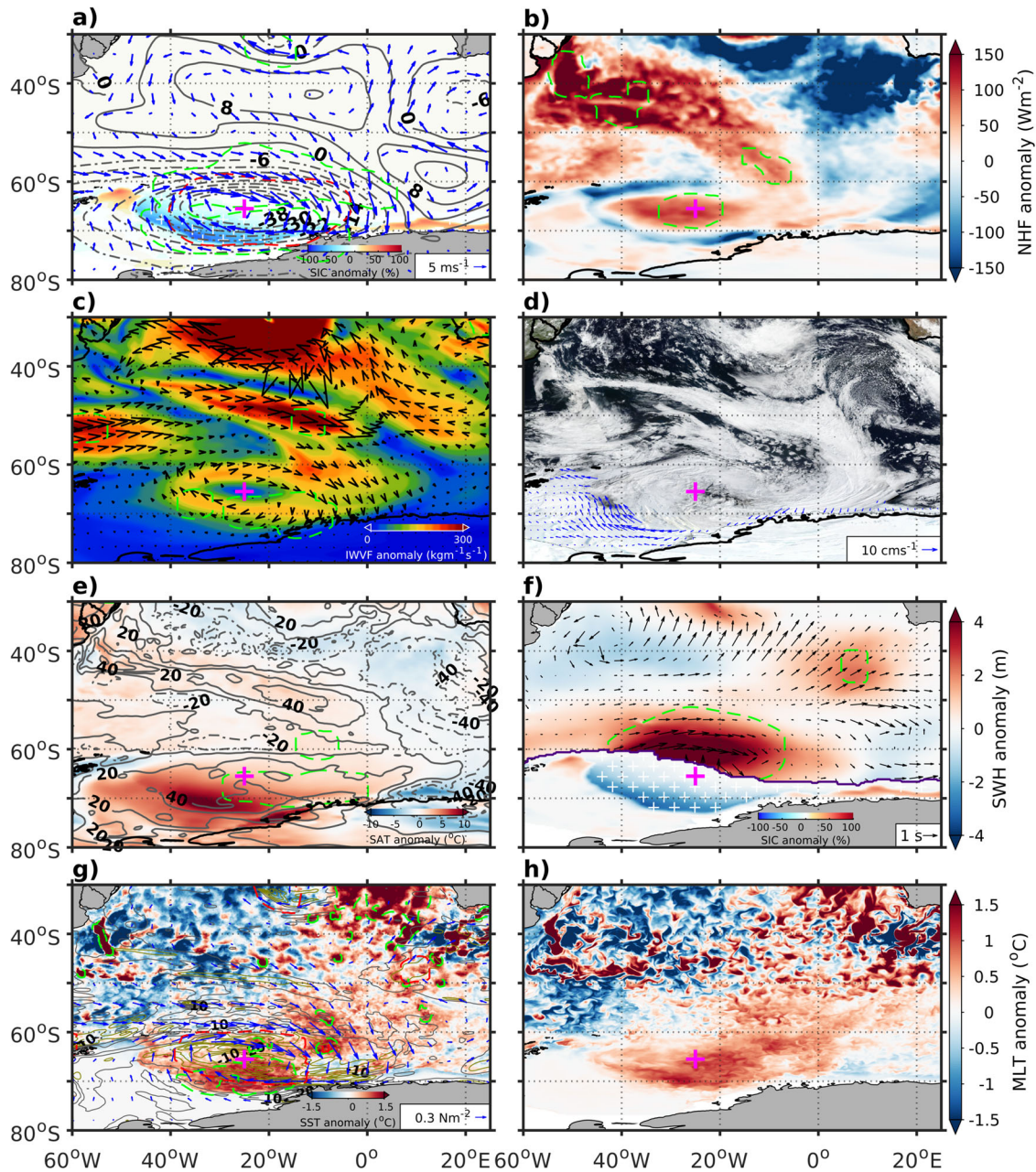


Fig. 3 Impact of the polar cyclone C1 on sea ice during 31 March 2019. **a** Anomalies of mean sea level pressure (MSLP) and wind vectors (blue arrows) are overlaid on anomalous sea ice concentration (SIC). Positive (negative) anomalies of MSLP are shown in solid (dashed) gray contours. The white plus marks showed the record low SIC values that remain outside from 1979 to 2020. **b–e** Anomalies in **(b)** net surface heat flux (NHF), **(c)** integrated water vapor flux (IWVF), **(d)** potential sea ice velocity (arrows) overlaid on cloud bands of cyclone from the Visible Infrared Imaging Radiometer Suite (VIIRS), **(e)** downward long-wave radiation (gray contours) overlaid on surface air temperature (SAT). **f** Significant wave height (SWH) anomalies are shown as color-shaded panel to the north of sea ice edge (purple line) with wave direction and period (black arrows) of combined wind waves and swells. The color-shaded panel to the south of the sea ice edge shows anomalous SIC. **g, h** Anomalies in **(g)** sea surface temperature (SST), wind stress vector (blue allows), negative wind stress curl (green contours, N m^{-3}), positive wind stress curl (gray contours) and **(h)** ocean mixed layer temperature (MLT). Regions within red (green) dashed polylines have record low (high) values that remain outside from 1979 to 2020. Within this, the record low is shown for MSLP and wind stress curl, while the record high is shown for other variables. The pink plus mark shows the low-pressure centre of the cyclone. The anomalies are computed relative to the climatology of 1979–2008.

the impact of cyclone C1 induced extreme changes in ocean-atmospheric conditions initiated the rapid decline in SIE ($0.024\text{--}0.032 \times 10^6 \text{ km}^2 \text{ day}^{-1}$) from 31 March to 4 April 2019 (Fig. 2c). It is also noted that the atmospheric rivers associated with polar cyclones bring enhanced precipitation⁶³ on sea ice cover which can slowdown the ice melting/reduction. Anomalously high precipitation ($\sim 1.13\text{--}2.72 \text{ cm}$) in form of snowfall was observed during the

occurrence of intense and explosive cyclones (Fig. 4d, Table 1). The slowdown of the ice melting/reduction occurs through enhanced snow accumulation which hinders the conduction-driven heat loss at the interface between ocean and sea ice. Also, the snowfall during the polar cyclones provides the freshwater influx to the ocean mixed layer that might have partly played a role by slowing down the ice melting/reduction.

Table 1. Characteristics of the polar cyclones (C1–C11) and its impact on sea ice through ocean-atmospheric variables.

1	2	3	4	5	6	7	8	9	10	11	12	13	14	15	16
Cyclones (NDR _i)	Date/Month (hrs) of 2019	Location	MSLP (hPa)	Du (days)	MSLP anomaly (hPa)	WS (m s ⁻¹)	SWH (m)	WSC (×10 ⁻⁵ N m ⁻³)	SST (°C)	SAT (°C)	IWVF (kg m ⁻¹ s ⁻¹)	DLR W m ⁻²	PR (cm)	NHF W m ⁻²	ΔSIE (10 ⁶ km ² day ⁻¹)
C1 (0.8746)	31/03 (00:00)	32.5°W, 65°S	931.41	7	-47.26	13.22 (22.05)	6.57 (9.64)	-0.45	2.12	10.07	244.4	51.63	1.13	112.84	-0.032
C2 (0.28179)	11/04 (06:00)	12.5°W, 65.75°S	951.67	7	-13.54	7.60 (15.46)	1.76 (4.66)	-0.60	2.49	13.96	284.4	67.33	4.84	242.00	-0.011
C3 (1.0039)	20/04 (18:00)	23°W, 62.25°S	941.80	9	-40.00	12.66 (21.3)	3.3 (6.95)	-0.50	2.01	11.83	312.7	63.10	1.82	112.75	-0.038
C4 (0.31131)	28-04 (00:00)	47.5°W, 70.5°S	967.40	5	-12.79	7.44 (14.37)	1.34 (4.94)	-0.49	2.55	11.75	204.3	64.59	4.78	165.39	-0.016
C5 (0.31868)	01/05 (06:00)	50.25°W, 69.75°S	962.59	5	-26.72	10.58 (15.50)	2.11 (4.64)	-0.28	2.56	16.57	264.4	95.47	0.99	147.60	-0.017
C6 (0.74874)	05/05 (06:00)	31.75°W, 64.5°S	965.47	9	-20.10	6.52 (14.72)	2.59 (5.19)	-0.20	2.91	13.20	330.3	68.81	1.45	137.18	-0.015
C7 (0.36011)	13/05 (00:00)	28.75°W, 69.5°S	964.88	6	-27.51	6.86 (15.06)	1.99 (5.09)	-0.28	2.53	13.79	175.4	71.16	0.79	127.03	-0.015
C8 (1.2946)	11/05 (06:00)	64°W, 63.5°S	943.89	5	-44.27	10.54 (16.30)	4.32 (6.80)	-0.45	2.66	15.19	235.3	81.12	2.72	152.73	-0.034
C9 (0.4224)	17/05 (12:00)	34.75°W, 67.5°S	955.95	5	-13.51	3.51 (12.78)	1.26 (4.26)	-0.18	2.49	12.74	238.8	58.47	0.83	111.11	-0.019
C10 (0.2787)	21/05 (12:00)	38.25°W, 62.75°S	954.88	5	-21.05	8.72 (17.09)	2.96 (6.28)	-0.70	2.72	15.26	109.1	74.04	1.73	90.09	-0.001
C11 (1.251)	25/05 (00:00)	15.25°W, 61.75°S	937.91	10	-41.54	13.91 (21.75)	4.80 (6.90)	-0.57	2.64	13.67	177.4	62.96	1.16	112.49	-0.026

Columns 1–4 represents the date and location of the cyclones while attaining a minimum central pressure in their life cycle. NDR_i is the relative central pressure normalized deepening rate computed for classification of the cyclones using 6 hourly mean sea level pressure (MSLP) from ERA5 (see the method, Atmospheric reanalysis). Bold type denotes intense and explosive cyclones (C1, C3, C8, C11) and bold italics are the quasi-stationary explosive cyclones (C3 and C11). Column 5 shows the duration of each cyclone (Du). Columns 6–16 indicates the daily extreme anomalies (minimum values are shown for MSLP, WSC and SIE; while, maximum for all other variables). Within this, the values in brackets are showing the absolute quantities. ΔSIE is the daily rate of change of sea ice extent (SIE) anomaly in response to cyclones.

WS Wind speed, SWH Significant wave height, WSC Wind stress curl, SST Sea surface temperature, SAT Surface air temperature, IWVF Integrated water vapor flux, DLR Downward long-wave radiation, PR Precipitation, NHF Net heat flux.

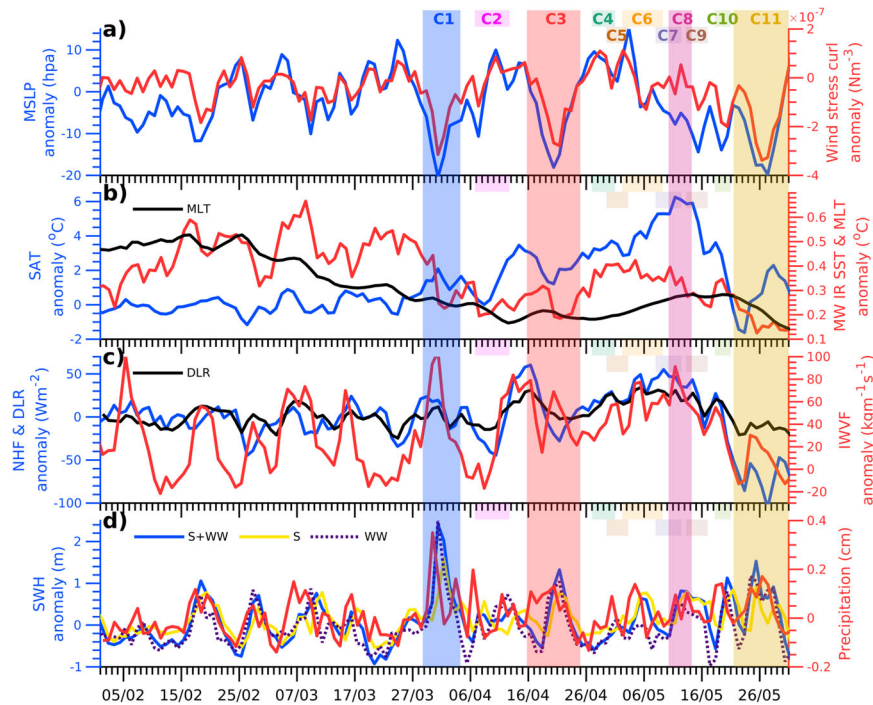


Fig. 4 Time series of ocean-atmospheric conditions during polar cyclones. Daily anomalies in (a) mean sea level pressure (MSLP), wind stress curl, (b) surface air temperature (SAT), ocean mixed layer temperature (MLT), sea surface temperature derived from blending of microwave and infrared observations (MW IR SST), (c) net heat flux (NHF), downward long-wave radiation (DLR), integrated water vapor flux (IWVF), (d) significant wave height (SWH, blue line) of combined wind waves (WW) and swells (yellow line), individual contributions from swells (yellow line), WW (dotted purple line) and total precipitation (red line) during 01 February–31 May 2019, spatially-averaged over the Weddell Sea within the green rectangle shown in Fig. 2a. The daily minimum and maximum anomalies of ocean-atmospheric variables are shown in Supplementary Fig. 4. Vertical color-shaded bars represent the occurrence period of cyclones (C1, C3, C8, C11) corresponding to the largest rate of sea ice changes in the Weddell Sea (See plus marks in Fig. 2c). The anomalies are computed relative to the climatology of 1979–2008.

Furthermore, a negative SIE anomaly was observed following the passage of cyclone C2 during 6 April–12 April 2019. Extreme atmospheric conditions associated with cyclone C2 were well observed by both automatic weather station (AWS) measurements and the ERA5 reanalysis, while the synoptic system was passing near a ship on 11–12 April 2019 (Supplementary Fig. 6). We find a close correspondence ($r = 0.84\text{--}0.99$, $p < 0.05$) between the AWS measurements and ERA5 data. The most rapid rate of decline in SIE anomalies occurred during the passage of explosive cyclone C3 during 16–25 April 2019.

Large decline in sea ice during the passage of explosive polar cyclones C3, C8 and C11

On 16 April 2019 a center of low MSLP (C3) with cyclonic wind pattern developed in the southwest Weddell Sea at $\sim 62^{\circ}\text{S}$ $\sim 48.75^{\circ}\text{W}$ (Supplementary Fig. 7). Low C3 followed an eastward trajectory from 16 April and remained quasi-stationary over the Weddell Sea during 18–22 April 2019 (Figs. 2a, 5a–d). At 6 UTC 19 April the cyclone was located at 69.5°S 40.5°W with a central MSLP of 966 hPa and a MSLP anomaly of ~ 34.8 hPa (Figs. 2b, 5a). The system rapidly deepened and attained a central pressure of 941 hPa (anomaly of ~ 40 hPa) and maximum sustained wind speed of 21.3 m s^{-1} at 18:00 UTC 20 April (Figs. 2b, 5b, Table 1). The relative central pressure NDR, within 24 h from 19 April to 20 April was more than a unity, and the system could be classified as an explosive cyclone (Table 1). The MSLP (wind speed) along the cyclone track for 16–25 April 2019, were the lowest (highest) ever recorded in the 42-year data from 1979 to 2020. Further, on 20 April, the explosive cyclone with a region of negative MSLP anomaly up to ~ 40 hPa extended over the entire Weddell Sea, was accompanied by positive MSLP anomaly (atmospheric blocking high) to the east extending meridionally from the South Atlantic

Ocean to the Lazarev Sea (Figs. 4a, 5a). The synoptic pattern directed southward flow of anomalous heat and moisture flux from the midlatitudes into the Weddell Sea over a meridional track that contributed to the sea ice decline (Fig. 5a–f). The IWVF reached up to 312 $\text{kg m}^{-1} \text{s}^{-1}$ all along the meridional track accompanied by an anomalous NHF up to ~ 112 W m^{-2} (Figs. 4c, 5e–f). The moisture plume analyzed by ERA5 and the cloud bands from the Visible-Infrared Imaging Radiometer Suite (VIIRS)/Suomi NPP during 20 April 2019, showed an atmospheric river¹⁹ extending from the South Atlantic Ocean into the Weddell Sea (Fig. 5f, g). A positive SAT anomaly of up to ~ 11.8 $^{\circ}\text{C}$ was observed over the Weddell Sea (Figs. 4b, 5h). The IWVF, NHF and SAT along the cyclone track on 20 April 2019 were the highest values ever recorded in the 42-year from 1979 to 2020. The nearby weather station at Troll (72°S 2.5°E , elevation 1284 m) in the Princess Martha Coast (Queen Maud Land), experienced an anomalous warming of 2.64 $^{\circ}\text{C}$ in April 2019. Similarly, Neumayer station (70.7°S 8.4°W , elevation 50 m) recorded an anomalous warming of 1.2 $^{\circ}\text{C}$. The poleward advection of warm air was the signature of the passage of a warm front indicating peaks in SAT¹⁸ (Figs. 4b, 5h). Also, the strong northerly winds associated with the cyclone dynamically forced the ice edge ~ 50 km southward with an advection velocity of ~ 0.58 m s^{-1} , thereby decreasing the SIE (Fig. 5g).

In parallel, the intense winds (~ 21.3 m s^{-1}) associated with cyclone C3 triggered the generation of high ocean waves that propagated toward to the sea ice edge (Figs. 5a–d, 6c–f). Prior to 20 April 2019, SWH up to ~ 4.2 m (anomaly of 2 m) was observed in the north-western part of the Weddell Sea, associated with the cyclonic winds during 16–17 April 2019 (Fig. 6a). Thereafter, the waves propagated southeastward with a gradual increase in SWH over the Weddell and Lazarev Seas as a result of the south-eastward track of the cyclone until 25 April (Fig. 6). The cyclone

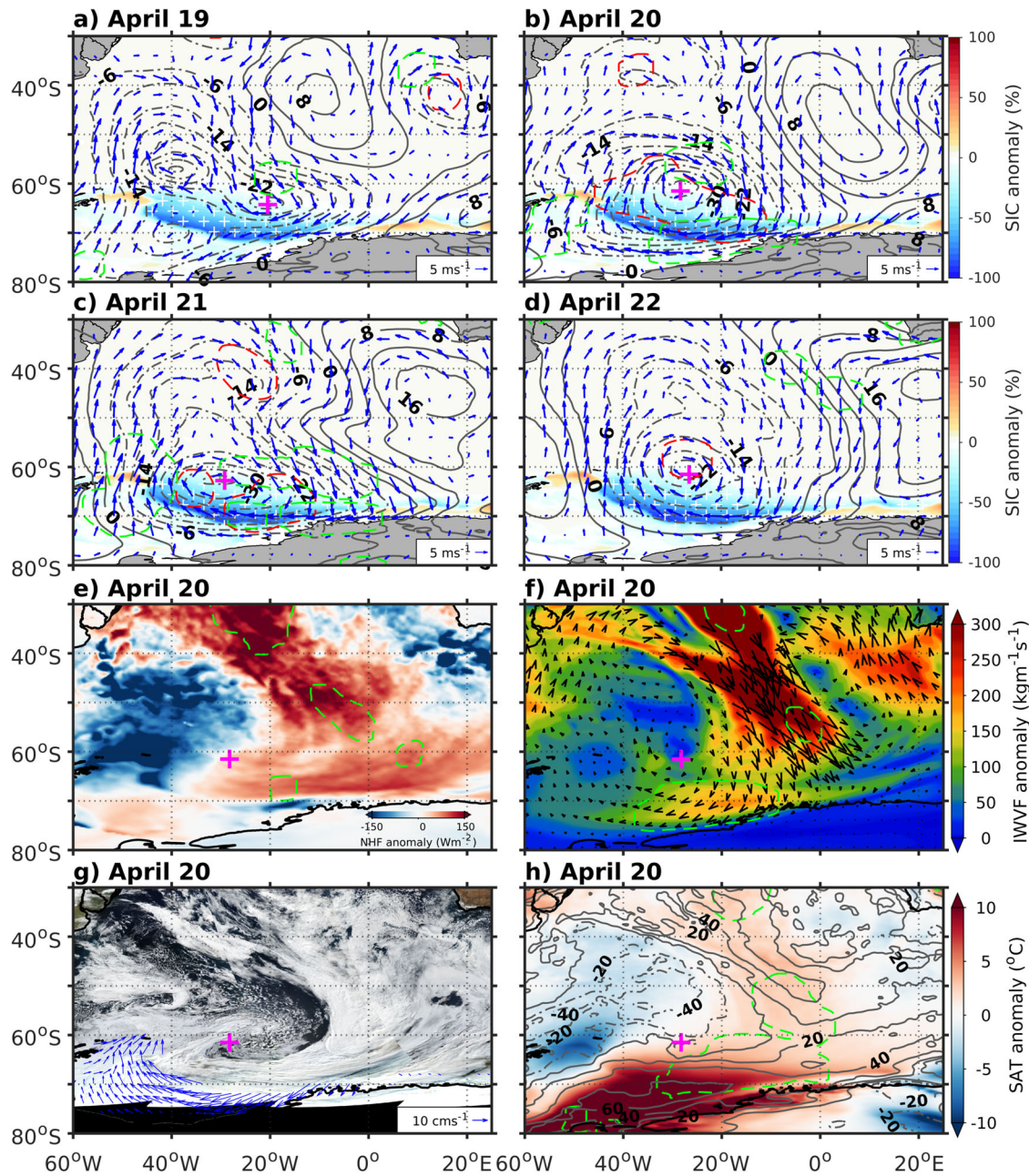


Fig. 5 Impact of the explosive cyclone C3 on sea ice. **a–d** Daily anomalies of mean sea level pressure (MSLP) and wind vectors (blue arrows) are overlaid on anomalous sea ice concentration (SIC) from 19 to 22 April 2019. Positive (negative) anomalies of MSLP are shown in solid (dashed) gray contours. The white plus marks showed the record low SIC values that remain outside from 1979 to 2020. **e–h** Anomalies in **(e)** net surface heat flux (NHF), **(f)** integrated water vapor flux (IWVF), **(g)** potential sea ice velocity (arrows) overlaid on cloud bands of cyclone from the Visible Infrared Imaging Radiometer Suite (VIIRS), and **(h)** downward long-wave radiation (gray contours) overlaid on surface air temperature (SAT) during explosive development on 20 April 2019. Regions within red (green) dashed polylines have record low (high) values that remain outside from 1979 to 2020. Within this, the record low is shown for MSLP, while the record high is shown for the other variables. The pink plus mark shows the low-pressure centre of the cyclone. The anomalies are computed relative to the climatology of 1979–2008.

was quasi-stationary over the Weddell Sea for 5 days (18–22 April 2019) with strong north to north-westerly winds of up to 21.3 m s^{-1} , which had a large fetch (Fig. 5a–d, Supplementary Fig. 8c–g). The strong winds during this long period provided a favorable environment for the formation of high waves that was leaving the fetch area as swell waves and propagated south-eastward into the marginal ice zone of the Weddell and Lazarev Seas (Fig. 6, Supplementary Fig. 9). The maximum SWH of $\sim 7 \text{ m}$ was generated near the sea ice edge with an anomaly of $\sim 3.3 \text{ m}$ during 19–22 April 2019 (Figs. 4d, 6c–f). The continuous south-eastward forcing

of wind waves and swells transferred momentum into the ice cover contributing to the break-up of the sea ice during the cyclonic episode. Also, the sea surface was forced by strong negative wind stress curl lower than $-0.5 \times 10^{-5} \text{ N m}^{-3}$ during the cyclone, which was conducive to upwelling and mixing of subsurface warm water into the surface (Figs. 4a, 7a–d). The upper ocean thermal structure showed anomalous warming of the SST and MLT up to $2.6 \text{ }^\circ\text{C}$ during the passage of cyclone C3 (Figs. 7, 4b, Supplementary Fig. 4b). As a result of extreme changes in ocean and atmospheric conditions during the lifetime of cyclone C3, the

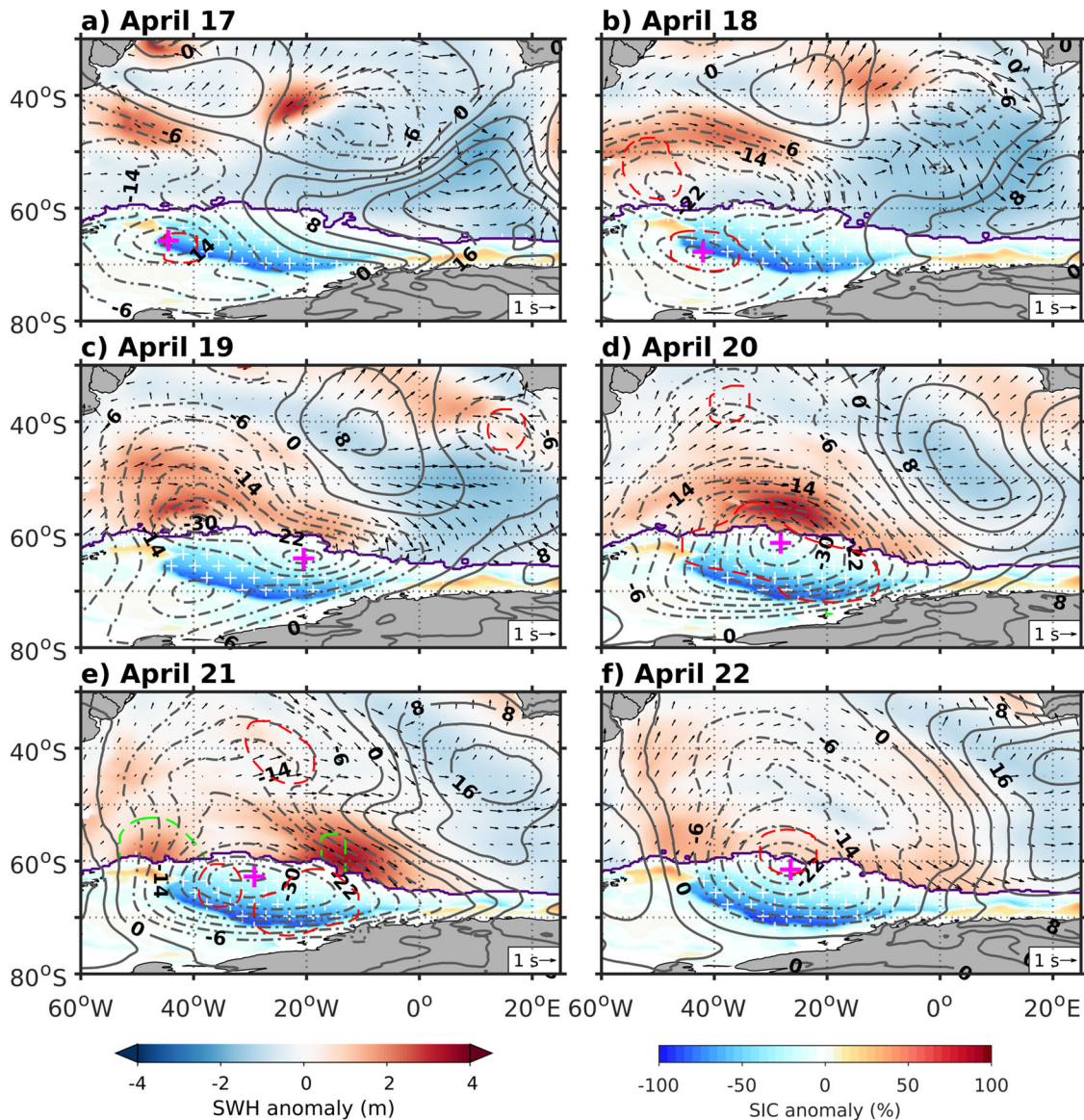


Fig. 6 Ocean waves–sea ice interaction during explosive cyclones. **a–f** Anomalies in daily significant wave height (SWH) shown in color-shaded panel to the north of sea ice edge (purple lines), with wave direction and period (black arrows) of combined wind waves and swells, mean sea level pressure (gray contours) are overlaid on anomalous sea ice concentration (SIC, color-shaded panel to the south of sea ice edge) during 17–22 April 2019 (Methods section ‘Ocean waves’). Regions within red (green) dashed polylines have record low (high) values that remain outside from 1979 to 2020. Within this, the record low is shown for MSLP, while the record high is shown for the SWH. The pink plus mark shows the low-pressure centre of the cyclone. The anomalies are computed relative to the climatology of 1979–2008.

most rapid rate of decline in SIE anomalies had occurred up to $0.038 \times 10^6 \text{ km}^2 \text{ day}^{-1}$.

The next largest rate of ice decline took place during the passage of explosive cyclone C8 over the southernmost latitudes ($>73^\circ\text{S}$) of the Weddell Sea, accompanied by a positive MSLP anomaly to its northeast during 11–15 May 2019 (Fig. 2a–c, Supplementary Fig. 10a). This explosive cyclone moving from the Bellingshausen Sea into the middle of the Weddell Sea with a central MSLP of 943 hPa (anomaly of 44.2 hPa) advected midlatitude warm air that led to the record high anomalous warming ($15\text{--}17.8^\circ\text{C}$) of SAT in the Weddell Sea during 11–15 May 2019 (Figs. 2b, 4a, b, Supplementary Fig. 4a, b). Similar to cyclones C1 and C3, the combined influence of extreme conditions in ocean–atmospheric parameters associated with the explosive cyclone C8 contributed to the rapid rate of SIE decline ($0.034 \times 10^6 \text{ km}^2 \text{ day}^{-1}$) during 11–15 May 2019 (Supplementary Fig. 10). During this period, the Weddell Sea SIE reached its lowest ever

anomalous extent ($-0.78\text{--}0.92 \times 10^6 \text{ km}^2$) in the satellite record, which was 24–26.3% lower than the long-term mean of 1979–2008 (Fig. 1a). It is not surprising that the largest rate of sea ice decline took place during the passage of a quasi-stationary explosive cyclone (C3) with its life cycle of ~ 9 days. In contrast, C8 which was a transient explosive cyclone with lesser life cycle (5 days), had a similar impact on sea ice because of its parallel movement close to the coast over the ice-covered region of the Weddell Sea (Table 1, Fig. 2a). Therefore, the proximity of the cyclone relative to the sea ice cover is important while assessing its impact on sea ice. Further, the ice extent continued to remain anomalously at record low levels ($0.75\text{--}0.87 \times 10^6 \text{ km}^2$) after the passage of another explosive cyclone (C11) with a central MSLP of up to 938 hPa (anomaly of 41.5 hPa) that caused poleward advection of heat and moisture fluxes into the Weddell Sea, high ocean waves and upper ocean warming during 22–31 May 2019 (Fig. 2a–c, Supplementary Fig. 11). In May 2019, the repeated

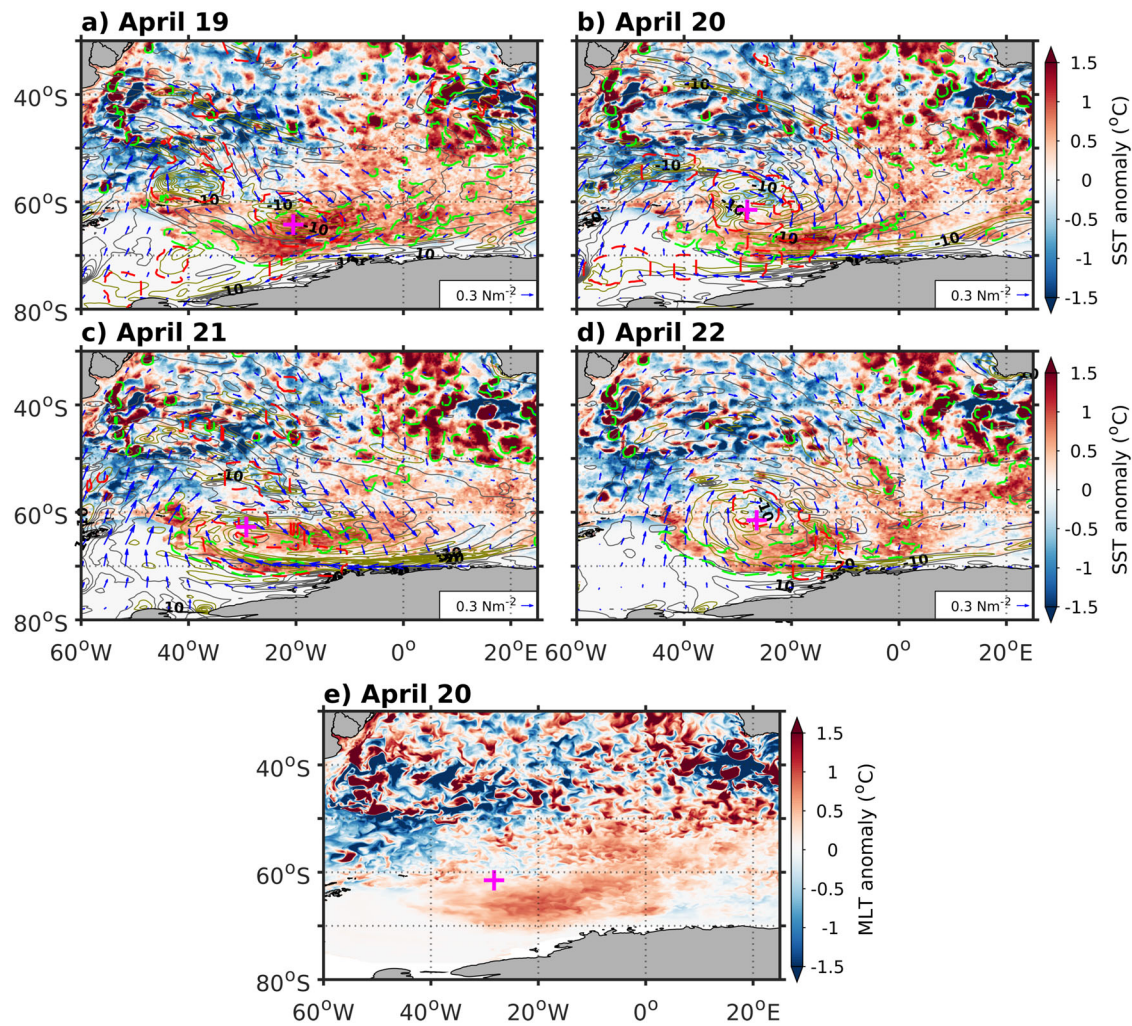


Fig. 7 Upper ocean thermal response to explosive cyclones. **a–d** Anomalies in sea surface temperature (SST), wind stress vectors (blue arrows), negative wind stress curl (green contours, N m^{-3}) and positive wind stress curl (gray contours) during 19–22 April 2019. **e** Ocean mixed layer temperature (MLT) anomaly during 20 April 2019 (see Methods section ‘Upper ocean temperature’). Regions within red (green) dashed polylines have record low (high) values that remain outside from 1979 to 2020. Within this, the record low is shown for wind stress curl, while the record high is shown for the ocean temperature. The pink plus mark shows the low-pressure centre of the cyclone. The anomalies are computed relative to the climatology of 1979–2008.

passage of polar cyclones, specifically the explosive developments over the Weddell Sea and their integrated impact on sea ice through ocean–atmospheric changes kept the ice extent lower than 21.2% from the long-term (1979–2008) mean value of $3.89 \times 10^6 \text{ km}^2$ (Fig. 1b).

Linkage of explosive developments to the large-scale atmospheric circulation

During February–March 2019, the atmospheric circulation over the entire Southern Ocean had a typical pattern of ZW3 in the geopotential height (GPH) anomaly at 500 hPa (Fig. 8a). The positive GPH anomaly centers were located roughly at the northwest of the AP ($\sim 82^\circ\text{W}$), west of Australia ($\sim 90^\circ\text{E}$), and southeast of New Zealand ($\sim 172^\circ\text{W}$) at a latitude of 50.5°S . The pattern of ZW3 was similar to the previous studies^{14,18} except the development of two cyclonic negative GPH anomalies in the Weddell and Lazarev Seas. The GPH in the Weddell and Lazarev Seas had negative anomalies that exceeded two standard deviations (sd) from the climatological mean. The position and depth of these low-pressure centers had a strong impact on the coastal Antarctica climatic conditions¹⁸.

During April 2019, the regions of negative GPH anomaly deepened in the interior of the Bellingshausen and Amundsen Seas (referred as Amundsen Sea Low, ASL^{64,65}) with the low pressure extending to the north of the Weddell Sea (Fig. 8b). To the east of the low-pressure zone, there was development of an atmospheric blocking high extending meridionally from southern Africa to the Lazarev Sea. The positive GPH anomalies exceeded 2 sd from the climatological mean. The east-to-west pressure gradient resulted in north-to-west westerly cyclonic flow with intrusion of heat and moisture from midlatitudes into the Weddell Sea that forced negative anomalies in regional sea ice conditions during April 2019 (Supplementary Fig. 12). Further, during May 2019, the negative GPH anomaly extended eastward over a large area in the Weddell Sea, with larger anomalies than April 2019, exceeding 2 sd (Fig. 8c). To the east of the low-pressure zone, the atmospheric blocking high had large GPH positive anomalies that exceeded 4 sd. The pressure field led to enhanced meridional flow of heat and moisture from midlatitudes into the Weddell Sea that led to anomalously low sea ice conditions in May 2019. The ZW3 index was in its positive phase for most of the days from March to May 2019 with pronounced amplification (Fig. 8d). The large zonal temperature gradients during the amplification of ZW3 leads to

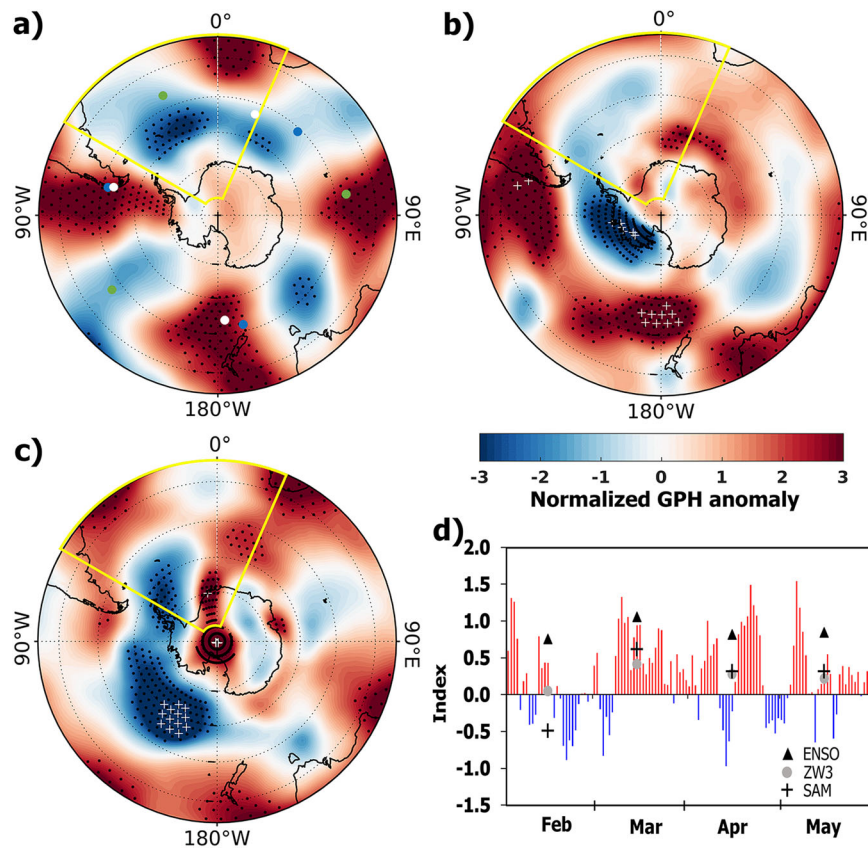


Fig. 8 Variability in zonal wave three (ZW3) index. Normalized anomalies of geopotential height at 500 hPa during (a) February–March 2019, (b) April 2019 and (c) May 2019, relative to the climatology of 1979–2008. Black dot (plus) marks showed the values that exceeded 2 (4) standard deviation from the climatological mean. White dots marked in figure-a represent the locations used for computing amplitudes of ZW3 index in the present study (Methods section ‘Atmospheric reanalysis’, Figure d). Locations used in the previous studies are shown in blue¹⁴ and green¹⁸ dots. Yellow box represents the Weddell Sea and surrounding region. **d** Daily changes in ZW3 index (red and blue bars) at three ridges (latitude 50.5°S; longitudes 18°E, 75°W, 172°E). Monthly mean SAM (plus marks) and ZW3 (circles) indices remained in positive phase, with a prevailing pattern of moderate El Niño events (triangles).

baroclinic instability that promotes genesis of explosive polar cyclones^{18,44} during April–May 2019. Therefore, on a daily time scale, the synoptic pattern of the ZW3 is similar to the extreme weather systems that influence the sea ice condition^{18,44}.

The amplification of zonal waves are often modulated by land-ocean temperature contrast and the major climate drivers like the SAM and the tropical Pacific ocean-atmospheric coupled phenomena like ENSO^{14,15,26,66,67}. There is an integrated impact of SAM and ENSO on preferential areas of zonal wave amplification, polar cyclones and sea ice that occurs through non-linear processes⁶⁸. However, it is complicated to identify a common causative factor that influences both SAM and ENSO, as they originate from different processes²⁶. In recent decades, SAM index showed an increasing trend toward high index polarity with the strengthening and poleward shifting of the westerly jet in austral summer²⁵. The polar stratosphere cooling (steepens north-south temperature gradient) owing to stratospheric ozone loss from anthropogenic emissions of ozone-depleting gases, leading to the increasing trend of SAM. The positive phase of SAM is known to deepen the ASL⁶⁴ which is a major feature of atmospheric zonal waves. During the study period, both the monthly mean SAM and ZW3 indices remained in positive phase, with a prevailing pattern of moderate El Niño events (Fig. 8d). SAM has significant ($p > 0.05$) out-of-phase correspondence with the sea level pressure over the Weddell Sea during April 2019; while, ENSO has significant ($p > 0.05$) in-phase relationship during February, March and May 2019 (Supplementary Fig. 12). Although, ENSO events might have

partly played a role on the zonal wave amplification around the Antarctica through propagation of atmospheric Rossby wave from tropics^{38,69}, the amplification due to natural variability of the polar circulation pattern¹⁶ is important for examining the underlying mechanism in the future work.

To summarize, we have examined the impact of a series of polar cyclones that forced an exceptional decline in SIE during April–May 2019. At the outset, the thermodynamic growth of sea ice in April–May 2019 was hindered by ocean preconditioning through anomalous warming of the mixed layer from the preceding summer of 2018/2019. This resulted from enhanced inputs of short-wave radiation due to the rare occurrence of an open ocean polynya^{11,40,41} and early melt of sea ice in the Weddell Sea³⁶. Within this scenario, eleven polar cyclones affected the Weddell Sea during the study period. These comprised four systems in April and seven in May 2019, which had an integrated impact on reducing the SIE. However, the rapid ice loss was primarily caused by the rapidly deepening intense and explosive cyclones (atmospheric bombs). The MSLP over a large area along the tracks of the such types of cyclones were the lowest ever recorded pressure in the 42-year data from 1979 to 2020, indicating the very rare nature of these events. The largest rate of change of SIE started during 31 March–4 April 2019, with the most rapid rate of decline during 16–19 April, 11–15 May and 22–31 May 2019 corresponding to the passage of intense and explosive cyclones. The cyclones had a marked impact by reducing the sea ice largely on their eastern flank, while increasing moderately on their western flank through

extreme changes in ocean-atmospheric conditions. With their associated northerly winds, the cyclones advected heat and moisture from midlatitudes (south Atlantic Ocean) into the Weddell Sea through atmospheric rivers that contributed to the anomalously low SIE. The record high wind speeds, IWVF, SAT, and heat flux gain by the ocean were pronounced over a large area in the Weddell Sea. The nearby Antarctica weather stations at the Troll and Neumayer recorded anomalous warming during this period.

The cyclones had an impact on the sea ice in terms of temperature and moisture variability on the scales of several days, but they also produced transient signals such as wind-induced wind-waves and swells that influenced the sea ice change. The eastward moving intense and explosive cyclones with strong northerly winds prevailed over a large fetch provided a favorable environment for the generation of high wind waves that propagated toward the marginal ice zone as swell. Very extreme sea state conditions in the Weddell Sea with record high wind waves and swell (height up to ~9.64 m) provided adequate energy to break-up the ice cover. In addition, the strong northerly winds dynamically forced the sea ice southward, further decreasing the ice extent. In parallel, the intense and explosive cyclone tracks were forced by record level negative wind stress curl that favored anomalous warming of the mixed layer thereby preventing thermodynamic growth of sea ice in the Weddell Sea. The SSTs along the cyclone track reached record high values over a large area during the intense and explosive developments. The underlying mechanism of mixed layer warming in this region is difficult to investigate using the current ocean reanalysis products, considering their uncertainty due to inadequate in-situ observations being ingested into the data assimilation. In summary, the combined influences of a series of eleven polar cyclones and mainly the explosive events induced dynamic (poleward swells, wind waves and ice drift) and thermodynamic (advection of heat and moisture fluxes from midlatitudes, ocean mixed layer warming) change providing a favorable condition for the rapid decline in sea ice over the Weddell Sea during April–May 2019. Consequently, the Weddell Sea SIE reached the fourth lowest extent in April 2019 and the lowest ever extent in May 2019. During this period, the atmospheric circulation anomalies were associated with a period of large amplitude tropospheric planetary waves, which resulted in enhanced meridional flow between midlatitudes and the Antarctic.

An analysis of polar cyclones and pressure depths over the Weddell Sea during 1979–2018 showed the occurrence of the deepest cyclones in 2016 and 2017, with record low pressure extremes reported at the Antarctic stations³⁶. The poleward displacement of midlatitude cyclones and increase in extreme cyclones in a warming climate^{70–74} is expected to have an increased impact on the Antarctic sea ice and regional climate. Most of the coupled climate models simulate a decline in the Antarctic sea ice since 1979 under a warming climate scenario⁷⁵, in contrast to moderate increase in SIE from satellite observations. Looking into the declining trend of sea ice from satellite observations during 2016–2020, it is difficult to provide a conclusive statement whether this trend is the start of the long-term decrease as predicted by various climate models. The recent sea ice decrease could be induced due to natural climate variability; however, the contribution from anthropogenic inputs cannot be discarded^{38,76}. Occurrence of anomalous explosive cyclones and their dynamic and thermodynamic impacts on sea ice are to be accounted in the climate models for projecting the long-term changes in sea ice and their climate feedback processes. This article identified the knowledge gaps in the existing approach such as why the polar cyclones play a crucial role, and act as one of the trigger in driving the interannual variability of Antarctic SIE.

METHODS

Sea ice observations

The sea ice observations from passive microwave satellite sensors are consistently available from 1979 and have been extensively used for the analysis of Antarctic climate. In order to examine the impact of polar cyclones on sea ice, we have used the daily and monthly mean SIC and SIE data derived from the Scanning Multichannel Microwave Radiometer (SMMR), the Special Sensor Microwave Imager (SSM/I), and the Special Sensor Microwave Imager Sounder at $0.25^\circ \times 0.25^\circ$ spatial resolution, available at the National Snow and Ice Data Center (NSIDC) (Data id–G02135 and NSIDC–0192, Version 3, <https://nsidc.org/>) for the period of 1979–2020. We analyzed the output of the NASA Team algorithm that computes SIC from the brightness temperatures of the three channels 19 V, 19H, and 37V^{77,78}. The SIE was computed after summing the areas of those pixels containing SIC values equals or more than 15%. The estimated accuracy of SIC from passive microwave satellite observations remains within 5% (15%) of the actual SIC in winter (summer). Detailed information on sensor characteristics, methodology of sea ice product generation, validation, and the limitations of retrieval methods are described in Fetterer et al., (2016). The satellite-derived sea ice observations were missing in each alternative day prior to 1987, and thus we filled the data gap for missing days after considering mean values between the previous and following available days. The daily and monthly anomaly in SIC and SIE over the Weddell Sea (60°W – 20°E and 55°S to Antarctic coast) were computed from 1 February to 31 May 2019, relative to the climatology of 1979–2008. The daily rate of change was computed from the difference of SIE anomaly for a given day from the preceding day. Record high and low values for all ocean-atmospheric variables were calculated for a specific day and month considering the entire time series of data corresponding to the same period from 1979 to 2020. We have analyzed the changes in SIA in addition to the SIE. However, the pattern of SIA variability is similar to SIE; therefore, we have considered only SIE in this study.

In-situ observations

The AWS unit onboard an ice-breaker cargo ship (MV Vasily Golovnin) recorded 6 hourly observations of MSLP, wind speed and air temperature at a height of 10 m above the sea level. The AWS data were available for 1 March to 26 April 2019, from 5.2°E to 12°E along the 69.5°S latitude. The AWS observations were combined with ERA5 products to assess the reliability of ERA5 during the passage of polar cyclones on sea ice cover. Mean bias error was calculated for ERA5 (dependent variables) while comparing with AWS observations (independent variables) recorded along the ship track [Eq. 1].

$$\text{Bias} = \frac{1}{n} \sum_{i=0}^n (\text{ERA5}_i - \text{AWS}_i) \quad (1)$$

A positive (negative) bias indicates the ERA5 was overestimated (underestimated) after comparison with the AWS data. We found very low bias in ERA5 variables and higher coefficient of correlation with AWS data (Supplementary Fig. 6). A close correspondence between AWS measurements and ERA5 indicated the reliability of ERA5 for studying the ocean-atmospheric variability during the passage of polar cyclones. It is noted that the AWS observations from the ship (MV Vasily Golovnin) were not assimilated in the ERA5. A low-pressure centre (<960 hPa) of cyclone C2 during 11–12 April 2019 passed within the region of ship movement, and therefore the extreme conditions are more prominent during this period as noticed from both AWS measurements and ERA5 (Supplementary Fig. 6). The correlation between the different ocean–atmospheric variables was computed using the Pearson correlation coefficients (r). The significance of the correlation was calculated at 95% confidence level ($p < 0.05$) using a two tailed statistical test.

Atmospheric reanalysis

In order to characterize the atmospheric circulation anomalies and polar cyclones, we analyzed the data from ECMWF ERA5⁷⁹. We used the MSLP, 10 m wind u and v components, 2 m SAT, IWVF, total precipitation, net incoming short-wave radiation (SWR), net outgoing long-wave radiation (OLR), downward long-wave radiation, sensible and latent heat flux available at a grid resolution of $0.25^\circ \times 0.25^\circ$ (www.ecmwf.int). We computed the net NHF after summing the net SWR, OLR, sensible and latent heat flux. The output positive (negative) values of NHF show heat gain (loss) by the ocean surface. Wind stress curl ($\nabla \times \boldsymbol{\tau}$) was calculated based up on the central differences for derivatives from ERA5 gridded data,

where τ is the wind stress [Eq. 2].

$$\nabla \times \tau = \frac{\partial \tau_y}{\partial x} - \frac{\partial \tau_x}{\partial y} \quad (2)$$

Cyclone tracking is a feature-based motion analysis; therefore, suitable low-pressure centre must be identified. Here, we have produced the 6 hourly cyclone tracks from ERA5 MSLP using a nearest neighbor method^{80,81} which connects the low-pressure centres in successive time intervals during 29 March–31 May 2019. The initial low for each cyclone in the study area was identified and the consecutive position of the low pressures during the next time step was found. In case of multiple positions during the next time step, the nearest neighbor to the current track has been considered to connect the track. After following this method, there were a total of eleven polar cyclones (named C1–C11) tracked over the Weddell Sea from 29 March to 31 May 2019 (Fig. 2a), that reached south of 60°S in their life cycle. In April 2019, four cyclones (C1–C4) were observed during the period of 29 March–04 April (C1), 06 April–12 April (C2), 16 April–25 April (C3) and 27 April–1 May (C4). In May 2019, seven cyclones (C5–C11) were observed during the period of 29 April–3 May (C5), 2 May–10 May (C6), 8 May–13 May (C7), 11 May–15 May (C8), 13 May–17 May (C9), 18 May–22 May (C10), and 22 May–31 May (C11). We categorized the synoptic system as an explosive polar cyclone or meteorological bomb when the relative central pressure NDR_r over 24 h exceeding unity. The NDR_r is computed using the following formula [Eq. 3]^{45,55,56}.

$$NDR_r = \frac{\Delta p_r \sin 60}{24 \text{ hPa} |\sin \phi|} \quad (3)$$

where, Δp_r is the change in relative central pressure over a period of 24 h, corresponding to the latitude ' ϕ '. We note that when a cyclone moves toward a climatological low-pressure zone, it experiences pseudo-deepening rate rather than actual deepening of the system. In order to eliminate this effect, the relative pressure was computed using the anomaly field from the long-term climatology (1979–2008). Of the eleven polar cyclones (C1–C11), there were three cyclones (C3, C8, C11) that could be categorized as explosive developments after following the above classification criteria (Fig. 2b, Table 1). Cyclone C1 was the most intense and deepened by >27 hPa in 24 h at 00 UTC 31 March at ~65°S ~32.5°W with a minimum central MSLP of 931 hPa (Figs. 2b, 3a, Table 1). However, the relative central pressure NDR_r over 24 h was less than a unity (~0.88), because of its movement into a climatological low-pressure zone. Such types of cyclones are categorized as an intense synoptic system^{41,82} when the central pressure drops below 950 hPa at 65°S. Although, this cyclone may not be exactly classified as a typical atmospheric bomb after following the methods from previous studies^{45,55,56}, but it's important to examine such unusual intense system (lowest ever recorded MSLP in the 42-year) which could initiate a large negative anomaly of sea ice through extreme changes in ocean-atmospheric parameters (Table 1, Fig. 3). The system C8 was formed as an explosive cyclone to the east of AP. The cloud patterns of the cyclones were studied from the visible band of VIIRS onboard the Suomi NPP.

The investigation of anomalous atmospheric conditions was carried out by computing the ZW3 index [Eq. 4]. ZW3 index affects the meridional transport of warm and cold air that influences the sea ice cover in polar regions. We have used the daily GPH (500 hPa) from ERA5 data to compute the ZW3 index at three ridges: latitude 50.5°S and longitude 18°E, 75°W, 172°E. The ZW3 index (I_z) is the average of values at three selected grid points, I_1 , I_2 , I_3 , where index is calculated as¹⁴:

$$I_z = \frac{X - \bar{X}}{\sigma_X} \quad (4)$$

For each grid point, X is the daily absolute value for the period, \bar{X} is the daily climatological mean (1979–2008), and σ_X is the daily standard deviation for the absolute values. The impact of ZW3 on sea ice occurs through changes in air temperature, heat, and moisture fluxes.

Ocean waves

To observe the ocean state during the study period, we have used ERA5 based significant wave height of combined wind waves and swell (SWH), SWH of total swell (SHTS), significant wave height of wind waves, mean direction of combined total swell, mean direction of wind waves, mean period of combined total swell, and mean period of wind waves at a grid resolution of 0.25° × 0.25°. The SWHs derived from several satellite

altimeters are the major source of observations have been used by ECMWF ERA5 for data assimilation^{83,84}. The atmosphere generates ocean waves in ECMWF Ocean Wave Model (ECWAM) through surface wind conditions, which in turn supplies surface roughness to boundary layer winds in the atmospheric model^{83–85}. ECWAM evaluates 2-d surface ocean wave spectrum where the spectrum under influence of local winds has been referred to as wind-waves and the remaining spectrum referred to as swells. The magnitude and direction from ECWAM simulated ocean waves in the Southern Ocean were found to be matching accurately with the buoy data and visual observations as per the WMO protocol⁴⁵.

Sea ice velocity

We have analyzed a reliable sea ice drift product with a spatial resolution of 0.25° × 0.25° available at NSIDC (<https://nsidc.org/data/NSIDC-0116/versions/4>)⁸⁶ for the period of 1979–2020. The input data sources from Advanced Very High-Resolution Radiometer, The Advanced Microwave Scanning Radiometer for EOS, SMMR, SSML, and SSML/S, buoys and the National Centers for Environmental Prediction (NCEP)/National Center for Atmospheric Research reanalysis forecasts are used to generate the sea ice drift product.

Upper ocean temperature

We have used the SST product with a spatial resolution of 0.25° × 0.25° available at Remote Sensing Systems (www.remss.com) for the period of 1998–2020, that was generated from integration of microwave and infrared sensor derived SST's (MW IR SST) after following an optimum interpolated (OI) method⁸⁷. The microwave frequencies can be used to derive SST in cloudy conditions, contrast to infrared wavelength measurements which are contaminated by the predominant cloud cover in the Southern Ocean. Yet, infrared measurements have higher spatial resolution than the SST from passive microwaves. Thus, the merging of SSTs from infrared and microwave provided a better synoptic coverage and resolution for the study region rather than using a single source. The errors in SST measurement from all the sensors are taken care of in the OI analysis. As the satellite derived SSTs provided information only from surface skin and sub-skin layer, we examined the vertical structure of potential temperature from the Copernicus Marine Environment Monitoring Service where in quality-controlled satellite and in-situ observations are being assimilated routinely (http://resources.marine.copernicus.eu/product-detail/GLOBAL_REANALYSIS_PHY_001_031/). The daily and monthly anomalies on potential temperature were computed for the period of January–May 2019, relative to the climatology of 1993–2008. The MLD was calculated as the depth for which the upper ocean potential density varies by 0.01 kg m⁻³ relative to the surface value⁸⁸.

Climate indices

We have used the SAM index⁸⁹ from the Climate Prediction Center (<ftp://ftp.cpc.ncep.noaa.gov/cwlinks/>) and the Nino3.4 anomalies using OI SST v2 product⁹⁰ available with a spatial resolution of 0.25° × 0.25° at NOAA/NCDC (https://climexp.knmi.nl/data/inino34_daily.dat).

DATA AVAILABILITY

Majority of the dataset used in this study are available freely and the links are provided in the 'Method Section'.

CODE AVAILABILITY

All the codes used in this study are available on request from the corresponding author.

Received: 26 August 2021; Accepted: 9 February 2022;

Published online: 18 March 2022

REFERENCES

- Morioka, Y., Doi, T., Iovino, D., Masina, S. & Behera, S. K. Role of sea-ice initialization in climate predictability over the Weddell Sea. *Sci. Rep.* **9**, 2457 (2019).
- Maksym, T. Arctic and Antarctic Sea Ice Change: Contrasts, Commonalities, and Causes. *Ann. Rev. Mar. Sci.* **11**, 187–213 (2019).

3. Weijer, W. et al. Local atmospheric response to an open-ocean polynya in a high-resolution climate model. *J. Clim.* **30**, 1629–1641 (2017).
4. Silvano, A. et al. Recent recovery of Antarctic Bottom Water formation in the Ross Sea driven by climate anomalies. *Nat. Geosci.* **13**, 780–786 (2020).
5. Zanowski, H., Hallberg, R. & Sarmiento, J. L. Abyssal Ocean Warming and Salinification after Weddell Polynyas in the GFDL CM2G Coupled Climate Model. *J. Phys. Oceanogr.* **45**, 2755–2772 (2015).
6. Naughten, K. A. et al. Modeling the Influence of the Weddell Polynya on the Filchner–Ronne Ice Shelf Cavity. *J. Clim.* **32**, 5289–5303 (2019).
7. Atkinson, A. et al. Krill (*Euphausia superba*) distribution contracts southward during rapid regional warming. *Nat. Clim. Chang.* **9**, 142–147 (2019).
8. Steinberg, D. K. et al. Long-term (1993–2013) changes in macrozooplankton off the Western Antarctic Peninsula. *Deep Sea Res. Part I Oceanogr. Res. Pap.* **101**, 54–70 (2015).
9. Arrigo, K. R., Brown, Z. W. & Mills, M. M. Sea ice algal biomass and physiology in the Amundsen Sea, Antarctica. *Elem. Sci. Anthr.* **2**, <https://doi.org/10.12952/journal.elementa.000028> (2014).
10. Tedesco, L. & Vichi, M. Sea ice biogeochemistry: a guide for modellers. *PLOS ONE* **9**, e89217 (2014).
11. Jena, B. & Anilkumar, N. P. Satellite observations of unprecedented phytoplankton blooms in the Maud Rise polynya, Southern Ocean. *Cryosphere* **14**, 1385–1398 (2020).
12. de Vos, M. et al. Evaluating numerical and free-drift forecasts of sea ice drift during a Southern Ocean research expedition: an operational perspective. *J. Oper. Oceanogr.* <https://doi.org/10.1080/1755876X.2021.1883293> (2021).
13. Parkinson, C. L. & Cavalieri, D. J. Antarctic sea ice variability and trends, 1979–2010. *Cryosphere* **6**, 871–880 (2012).
14. Raphael, M. N. A zonal wave 3 index for the Southern Hemisphere. *Geophys. Res. Lett.* **31**, L23212 (2004).
15. Raphael, M. N. The influence of atmospheric zonal wave three on Antarctic sea ice variability. *J. Geophys. Res. Atmos.* **112**, D12112 (2007).
16. Turner, J., Harangozo, S. A., Marshall, G. J., King, J. C. & Colwell, S. R. Anomalous atmospheric circulation over the Weddell Sea, Antarctica during the Austral summer of 2001/02 resulting in extreme sea ice conditions. *Geophys. Res. Lett.* **29**, 2160 (2002).
17. Turner, J., Hosking, J. S., Bracegirdle, T. J., Phillips, T. & Marshall, G. J. Variability and trends in the Southern Hemisphere high latitude, quasi-stationary planetary waves. *Int. J. Climatol.* **37**, 2325–2336 (2017).
18. Francis, D., Eayrs, C., Cuesta, J. & Holland, D. Polar Cyclones at the Origin of the Reoccurrence of the Maud Rise Polynya in Austral Winter 2017. *J. Geophys. Res. Atmos.* **124**, 5251–5267 (2019).
19. Francis, D., Mattingly, K. S., Temimi, M., Massom, R. & Heil, P. On the crucial role of atmospheric rivers in the two major Weddell Polynya events in 1973 and 2017 in Antarctica. *Sci. Adv.* **6**, eabc2695 (2020).
20. Bintanja, R., Van Oldenborgh, G. J., Drijfhout, S. S., Wouters, B. & Katsman, C. A. Important role for ocean warming and increased ice-shelf melt in Antarctic sea-ice expansion. *Nat. Geosci.* **6**, 376–379 (2013).
21. Haumann, F. A., Gruber, N., Münnich, M., Frenger, I. & Kern, S. Sea-ice transport driving Southern Ocean salinity and its recent trends. *Nature* **537**, 89–92 (2016).
22. Holland, P. R. & Kwok, R. Wind-driven trends in Antarctic sea-ice drift. *Nat. Geosci.* **5**, 872–875 (2012).
23. Turner, J. et al. Non-annular atmospheric circulation change induced by stratospheric ozone depletion and its role in the recent increase of Antarctic sea ice extent. *Geophys. Res. Lett.* **36**, L08502 (2009).
24. Ferreira, D., Marshall, J., Bitz, C. M., Solomon, S. & Plumb, A. Antarctic ocean and sea ice response to ozone depletion: A two-time-scale problem. *J. Clim.* **28**, 1206–1226 (2015).
25. Thompson, D. W. J. et al. Signatures of the Antarctic ozone hole in Southern Hemisphere surface climate change. *Nat. Geosci.* **4**, 741–749 (2011).
26. Pezza, A. B., Rashid, H. A. & Simmonds, I. Climate links and recent extremes in antarctic sea ice, high-latitude cyclones, Southern Annular Mode and ENSO. *Clim. Dyn.* **38**, 57–73 (2012).
27. Stammerjohn, S. E., Martinson, D. G., Smith, R. C., Yuan, X. & Rind, D. Trends in Antarctic annual sea ice retreat and advance and their relation to El Niño–Southern Oscillation and Southern Annular Mode variability. *J. Geophys. Res.* **113**, C03590 (2008).
28. Doddridge, E. W. & Marshall, J. Modulation of the Seasonal Cycle of Antarctic Sea Ice Extent Related to the Southern Annular Mode. *Geophys. Res. Lett.* **44**, 9761–9768 (2017).
29. Holland, M. M., Landrum, L., Kostov, Y. & Marshall, J. Sensitivity of Antarctic sea ice to the Southern Annular Mode in coupled climate models. *Clim. Dyn.* **49**, 1813–1831 (2017).
30. Matear, R. J., O’Kane, T. J., Risbey, J. S. & Chamberlain, M. Sources of heterogeneous variability and trends in Antarctic sea-ice. *Nat. Commun.* **6**, 8656 (2015).
31. Paolo, F. S. et al. Response of Pacific-sector Antarctic ice shelves to the El Niño/Southern Oscillation. *Nat. Geosci.* **11**, 121–126 (2018).
32. Turner, J. et al. Extreme temperatures in the Antarctic. *J. Clim.* **34**, 2653–2668 (2021).
33. Yu, L.-J., Zhong, S.-Y., Sui, C.-J., Zhang, Z.-R. & Sun, B. Synoptic mode of Antarctic summer sea ice superimposed on interannual and decadal variability. *Adv. Clim. Chang. Res.* **12**, 147–161 (2021).
34. Sigmond, M. & Fyfe, J. C. The antarctic sea ice response to the ozone hole in climate models. *J. Clim.* **27**, 1336–1342 (2014).
35. Sigmond, M. & Fyfe, J. C. Has the ozone hole contributed to increased Antarctic sea ice extent? *Geophys. Res. Lett.* **37**, L18502 (2010).
36. Turner, J. et al. Recent Decrease of Summer Sea Ice in the Weddell Sea, Antarctica. *Geophys. Res. Lett.* **47**, e2020GL087127 (2020).
37. Turner, J. et al. Unprecedented springtime retreat of Antarctic sea ice in 2016. *Geophys. Res. Lett.* **44**, 6868–6875 (2017).
38. Eayrs, C., Li, X., Raphael, M. N. & Holland, D. M. Rapid decline in Antarctic sea ice in recent years hints at future change. *Nat. Geosci.* **14**, 460–464 (2021).
39. Simmonds, I. & Li, M. Trends and variability in polar sea ice, global atmospheric circulations, and baroclinicity. *Ann. N. Y. Acad. Sci.* **1504**, 167–186 (2021).
40. Jena, B., Ravichandran, M. & Turner, J. Recent Reoccurrence of Large Open-Ocean Polynya on the Maud Rise Seamount. *Geophys. Res. Lett.* **46**, 4320–4329 (2019).
41. Campbell, E. C. et al. Antarctic offshore polynyas linked to Southern Hemisphere climate anomalies. *Nature* **570**, 319–325 (2019).
42. van Loon, H. & Jenne, R. L. The zonal harmonic standing waves in the southern hemisphere. *J. Geophys. Res.* **77**, 992–1003 (1972).
43. Irving, D. & Simmonds, I. A novel approach to diagnosing Southern Hemisphere planetary wave activity and its influence on regional climate variability. *J. Clim.* **28**, 9041–9057 (2015).
44. Francis, D., Mattingly, K. S., Lhermitte, S., Temimi, M. & Heil, P. Atmospheric extremes caused high oceanward sea surface slope triggering the biggest calving event in more than 50 years at the Amery Ice Shelf. *Cryosphere* **15**, 2147–2165 (2021).
45. Vichi, M. et al. Effects of an Explosive Polar Cyclone Crossing the Antarctic Marginal Ice Zone. *Geophys. Res. Lett.* **46**, 5948–5958 (2019).
46. Woods, C. & Caballero, R. The role of moist intrusions in winter arctic warming and sea ice decline. *J. Clim.* **29**, 4473–4485 (2016).
47. Finocchio, P. M., Doyle, J. D., Stern, D. P. & Fearon, M. G. Short-term Impacts of Arctic Summer Cyclones on Sea Ice Extent in the Marginal Ice Zone. *Geophys. Res. Lett.* **47**, e2020GL088338 (2020).
48. Uotila, P. et al. Relationships between Antarctic cyclones and surface conditions as derived from high-resolution numerical weather prediction data. *J. Geophys. Res. Atmos.* **116**, D07109 (2011).
49. Kohout, A. L., Williams, M. J. M., Dean, S. M. & Meylan, M. H. Storm-induced sea-ice breakup and the implications for ice extent. *Nature* **509**, 604–607 (2014).
50. Squire, V. A. Ocean Wave Interactions with Sea Ice: a reappraisal. *Annu. Rev. Fluid Mech.* **52**, 37–60 (2020).
51. Aouf, L. et al. New Directional Wave Satellite Observations: towards Improved Wave Forecasts and Climate Description in Southern Ocean. *Geophys. Res. Lett.* **48**, e2020GL091187 (2021).
52. Muench, R. D. Relict Convective Features in the Weddell Sea. in *Deep Convection and Deep Water Formation in the Oceans* (eds. Chu, P. C. & Gascard, J. C. B. T.-E. O. S.) **57**, 53–67 (Elsevier, 1991).
53. Cheon, W. G. et al. Replicating the 1970s’ Weddell Polynya using a coupled ocean-sea ice model with reanalysis surface flux fields. *Geophys. Res. Lett.* **42**, 5411–5418 (2015).
54. Casas-Prat, M. & Wang, X. L. Sea Ice Retreat Contributes to Projected Increases in Extreme Arctic Ocean Surface Waves. *Geophys. Res. Lett.* **47**, e2020GL088100 (2020).
55. Reale, M. et al. A Global Climatology of Explosive Cyclones using a Multi-Tracking Approach. *Tellus A Dyn. Meteorol. Oceanogr.* **71**, <https://doi.org/10.1080/16000870.2019.1611340> (2019).
56. Lim, E. P. & Simmonds, I. Explosive cyclone development in the Southern Hemisphere and a comparison with Northern Hemisphere events. *Mon. Weather Rev.* **130**, 2188–2209 (2002).
57. Sato, K. & Simmonds, I. Antarctic skin temperature warming related to enhanced downward longwave radiation associated with increased atmospheric advection of moisture and temperature. *Environ. Res. Lett.* **16**, 064059 (2021).
58. Wassermann, S., Schmitt, C., Kottmeier, C. & Simmonds, I. Coincident vortices in Antarctic wind fields and sea ice motion. *Geophys. Res. Lett.* **33**, L15810 (2006).
59. Dolatshah, A. et al. Letter: Hydroelastic interactions between water waves and floating freshwater ice. *Phys. Fluids* **30**, 091702 (2018).
60. Montiel, F. & Squire, V. A. Modelling wave-induced sea ice break-up in the marginal ice zone. *Proc. R. Soc. A Math. Phys. Eng. Sci.* **473**, 20170258 (2017).
61. Stopa, J. E., Sutherland, P. & Ardhuin, F. Strong and highly variable push of ocean waves on Southern Ocean sea ice. *Proc. Natl Acad. Sci.* **115**, 5861–5865 (2018).

62. de Steur, L., Holland, D. M., Muench, R. D. & McPhee, M. G. The warm-water 'Haló' around Maud Rise: properties, dynamics and Impact. *Deep. Res. Part I Oceanogr. Res. Pap.* **54**, 871–896 (2007).
63. Schreiber, E. A. P. & Serreze, M. C. Impacts of synoptic-scale cyclones on Arctic sea-ice concentration: a systematic analysis. *Ann. Glaciol.* **61**, 139–153 (2020).
64. Turner, J., Phillips, T., Hosking, J. S., Marshall, G. J. & Orr, A. The Amundsen Sea low. *Int. J. Climatol.* **33**, 1818–1829 (2013).
65. Raphael, M. N. et al. The Amundsen sea low: Variability, change, and impact on Antarctic climate. *Bull. Am. Meteorol. Soc.* **97**, 111–121 (2016).
66. Renwick, J. A. Southern Hemisphere circulation and relations with sea ice and sea surface temperature. *J. Clim.* **15**, 3058–3068 (2002).
67. Screen, J. A., Bracegirdle, T. J. & Simmonds, I. Polar Climate Change as Manifest in Atmospheric Circulation. *Curr. Clim. Chang. Rep.* **4**, 383–395 (2018).
68. Khokhlov, V. N., Glushkov, A. V. & Loboda, N. S. On the nonlinear interaction between global teleconnection patterns. *Q. J. R. Meteorol. Soc.* **132**, 447–465 (2006).
69. Stuecker, M. F., Bitz, C. M. & Armour, K. C. Conditions leading to the unprecedented low Antarctic sea ice extent during the 2016 austral spring season. *Geophys. Res. Lett.* **44**, 9008–9019 (2017).
70. Fyfe, J. C. Extratropical Southern Hemisphere cyclones: Harbingers of climate change? *J. Clim.* **16**, 2802–2805 (2003).
71. Bengtsson, L., Hodges, K. I. & Keenlyside, N. Will extratropical storms intensify in a warmer climate? *J. Clim.* **22**, 2276–2301 (2009).
72. Chang, E. K. M., Guo, Y. & Xia, X. CMIP5 multimodel ensemble projection of storm track change under global warming. *J. Geophys. Res. Atmos.* **117**, D23118 (2012).
73. Tamarin, T. & Kaspi, Y. The poleward shift of storm tracks under global warming: a Lagrangian perspective. *Geophys. Res. Lett.* **44**, 10,666–10,674 (2017).
74. Grieger, J., Leckebusch, G. C., Raible, C. C., Rudeva, I. & Simmonds, I. Subantarctic cyclones identified by 14 tracking methods, and their role for moisture transports into the continent. *Tellus A Dyn. Meteorol. Oceanogr.* **70**, 1–18 (2018).
75. Polvani, L. M. & Smith, K. L. Can natural variability explain observed Antarctic sea ice trends? New modeling evidence from CMIP5. *Geophys. Res. Lett.* **40**, 3195–3199 (2013).
76. Wang, G. et al. Compounding tropical and stratospheric forcing of the record low Antarctic sea-ice in 2016. *Nat. Commun.* **10**, 13 (2019).
77. Cavalieri, D. J., Parkinson, C. L., Gloersen, P. & Zwally, H. J. *Arctic and Antarctic Sea Ice Concentrations from Multichannel Passive-Microwave Satellite Data Sets: October 1978–September 1995 - User's Guide. NASA TM 104647.* (1997).
78. Fetterer, F., Knowles, K., Meier, W. & Savoie, M. *Sea Ice Index, Version 2 (updated daily). NSIDC: National Snow and Ice Data Center. Boulder, Colorado USA.* <https://doi.org/10.7265/N5736NV7> (2016)
79. Hersbach, H. et al. *ERA5 monthly averaged data on single levels from 1979 to present. Copernicus Climate Change Service (C3S) Climate Data Store (CDS). Fire Prevention and Fire Engineers Journals* (2019). <https://doi.org/10.24381/cds.adbb2d47>
80. Hodges, K. I. A General Method for Tracking Analysis and Its Application to Meteorological Data. *Mon. Weather Rev.* **122**, 2573–2586 (1994).
81. Xia, B. L., Zahn, M., Hodges, K. I., Feser, F. & Storch, H. Von. A comparison of two identification and tracking methods for polar lows. *Tellus, Ser. A Dyn. Meteorol. Oceanogr.* **64**, <https://doi.org/10.3402/tellusa.v64i0.17196> (2012).
82. Patoux, J., Yuan, X. & Li, C. Satellite-based midlatitude cyclone statistics over the Southern Ocean: 1. Scatterometer-derived pressure fields and storm tracking. *J. Geophys. Res. Atmos.* **114**, D04105 (2009).
83. Abdalla, S., Dinardo, S., Benveniste, J. & Janssen, P. A. E. M. Assessment of CryoSat-2 SAR mode wind and wave data. *Adv. Sp. Res.* **62**, 1421–1433 (2018).
84. Hersbach, H. et al. The ERA5 global reanalysis. *Q. J. R. Meteorol. Soc.* **146**, 1999–2049 (2020).
85. Simmons, A. et al. Low frequency variability and trends in surface air temperature and humidity from ERA5 and other datasets. *ECMWF Tech. Memoranda* **881**, 6–7. <https://doi.org/10.21957/ly5vbtbfd> (2021).
86. Tschudi, M., Meier, W. N., Stewart, J. S., Fowler, C. & Maslanik, J. Polar Pathfinder Daily 25 km EASE Grid Sea Ice Motion Vectors, Version 4. Boulder, Colorado USA. NASA National Snow and Ice Data Center Distributed Active Archive Center. <https://doi.org/10.5067/INAWUWO7QH7B> (2019).
87. Reynolds, R. W. & Smith, T. M. Improved global sea surface temperature analyses using optimum interpolation. *J. Clim.* **7**, 929–948 (1994).
88. Kaufman, D. E., Friedrichs, M. A. M., Smith, W. O., Queste, B. Y. & Heywood, K. J. Biogeochemical variability in the southern Ross Sea as observed by a glider deployment. *Deep. Res. Part I Oceanogr. Res. Pap.* **92**, 93–106 (2014).
89. Mo, K. C. Relationships between low-frequency variability in the Southern Hemisphere and sea surface temperature anomalies. *J. Clim.* **13**, 3599–3610 (2000).
90. Reynolds, R. W. et al. Daily high-resolution-blended analyses for sea surface temperature. *J. Clim.* **20**, 5473–5496 (2007).

ACKNOWLEDGEMENTS

We acknowledge Director, National Centre for Polar and Ocean Research, for providing necessary support. The Ministry of Earth Sciences, Government of India, is acknowledged for funding support. We acknowledge data made available by various centres, including the National Snow and Ice Data Center, European Centre for Medium-range Weather Forecast, Copernicus Marine Environment Monitoring Service, National Aeronautics and Space Administration, National Oceanic and Atmospheric Administration, and their processing teams for providing various datasets via their portals. Thanks to the editor and three anonymous reviewers for conducting a rigorous peer-review process that helped to improve the quality of the paper. This is NCPOR contribution number J-80/2021-22.

AUTHOR CONTRIBUTIONS

B.J. Idea formulation, design of methodology, analysis, interpretation, and wrote the paper. All six authors contributed for the development of the study, analysis, interpretation, review, and editing.

COMPETING INTERESTS

We declare that we have no known competing financial interests (covering both financial and non-financial interests) or personal relationships that could have appeared to influence the work reported in this paper.

ADDITIONAL INFORMATION

Supplementary information The online version contains supplementary material available at <https://doi.org/10.1038/s41612-022-00243-9>.

Correspondence and requests for materials should be addressed to B. Jena.

Reprints and permission information is available at <http://www.nature.com/reprints>

Publisher's note Springer Nature remains neutral with regard to jurisdictional claims in published maps and institutional affiliations.



Open Access This article is licensed under a Creative Commons Attribution 4.0 International License, which permits use, sharing, adaptation, distribution and reproduction in any medium or format, as long as you give appropriate credit to the original author(s) and the source, provide a link to the Creative Commons license, and indicate if changes were made. The images or other third party material in this article are included in the article's Creative Commons license, unless indicated otherwise in a credit line to the material. If material is not included in the article's Creative Commons license and your intended use is not permitted by statutory regulation or exceeds the permitted use, you will need to obtain permission directly from the copyright holder. To view a copy of this license, visit <http://creativecommons.org/licenses/by/4.0/>.

© The Author(s) 2022